

Adjoint-based control of loud events in a turbulent jet

Jeonglae Kim¹, Daniel J. Bodony² and Jonathan B. Freund^{1,2,†}

¹Department of Mechanical Science and Engineering, University of Illinois at Urbana-Champaign, 1206 W. Green Street, Urbana, IL 61801, USA

²Department of Aerospace Engineering, University of Illinois at Urbana-Champaign, 104 S. Wright Street, Urbana, IL 61801, USA

(Received 30 April 2013; revised 30 September 2013; accepted 6 December 2013)

Efforts to reduce the noise from turbulent jets at fixed flow conditions, with aircraft noise as the principal technological motivation, have generally involved some degree of parametric empiricism often based upon a series of trial-and-error testing. As a result, it is unclear if the modest reductions found, in rare cases that do not greatly affect the flow field or incur prohibitive losses, are near the limit of what can be accomplished or if there are undiscovered opportunities for more substantive reductions with better designs or active control. We assess this using an adjoint-based optimization procedure in conjunction with an experimentally validated large-eddy simulation of a Mach 1.3 turbulent jet. The adjoint solution provides a definitive direction in which to adjust a model control actuation in order to reduce noise, providing guidance that seems lacking by any other current means. It is found that three conjugate-gradient iterations in the control space provide ~ 3.5 dB of reduction, comparable to other reductions found empirically. The control seems to work by disrupting the coherence of acoustically efficient axisymmetric flow structures. The control and noise-reduction mechanisms are informative, but also suggest that any significantly quieter state would not be a simple perturbation from the uncontrolled jet. Additional iterations might reduce noise more significantly, but there might be only modest opportunities to reduce the sound from simple round turbulent jets without radical changes or relatively sophisticated controls. Though it is difficult to prove any behaviour in a global space of actuations, there does not seem to be a direct route based upon a local sensitivity gradient to substantially quieting a jet, even with an unrealistically flexible actuation. More complex jets or other noisy flows may be more amenable to control, in which case the adjoint-based optimization procedure demonstrated here could provide invaluable engineering guidance.

Key words: aeroacoustics, jet noise, noise control

1. Introduction

Jet noise reduction is important for the contemporary aviation industry, which faces significant noise limits that precipitate demands for ever quieter aircraft. Though the

†Email address for correspondence: jbfreund@illinois.edu

flow turbulence in the jet plume is responsible for a significant portion of jet noise, it has defied a simplified description with sufficient fidelity to reliably guide reduction efforts. Detailed simulation, either directly without modelling approximation (Freund, Lele & Moin 2000; Freund 2001) or with subgrid-scale models for smaller turbulence scales (Bodony & Lele 2005, 2008; Uzun & Hussaini 2009; Karabasov *et al.* 2010; Bogey, Marsden & Bailly 2012; Lo *et al.* 2012), has recently been able to provide viable predictions. These predictions, including their full space–time databases, have been useful to explain certain jet noise source properties, but they have not yet yielded sufficient guidance on how to reduce jet noise. Similarly, recent experimental investigations have demonstrated the viability of some noise reduction methodologies (Bridges & Brown 2004; Samimy *et al.* 2010); however, they are not founded upon detailed cause-and-effect relationships between the altered near-field turbulence and the quieted far field. This conceptual difficulty derives directly from our inability to separate out the noise source from the compressible turbulent flow in which it is embedded. It is a manifestation of the descriptive challenge of turbulence.

Theoretical descriptions, which provide an analogy between turbulence statistics and externally applied noise sources (Lighthill 1952; Goldstein 2003) show the basic inefficiency of turbulence noise sources. In the zero Mach number limit, the source is quadrupole in character, with radiation arising only via weak non-self-cancelling components of the nominal noise source. In subsonic flows, most of this source has a wavenumber–frequency make-up that does not couple with radiating acoustic waves (Ffowcs Williams 1963). While these factors make prediction challenging, they also suggest that jet noise reduction can be accomplished without suppressing turbulence *per se*, but instead by making it less acoustically efficient. Means of doing this are not necessarily easier to identify, but we can anticipate that they might require a relatively modest and therefore easier-to-accomplish change to the turbulence. Doing this under the controlled circumstances provided by a detailed simulation of genuinely chaotic turbulence is the goal of this paper. Given that the theoretical sound sources can be described by high-order statistics of turbulence fluctuations that are not easily interpreted, the viability of such an approach seems currently to require such a detailed simulation description of the flow. We anticipate that experiments and engineering design might eventually be integrated within such an approach, but present limitations in actuation or nozzle geometry design mean that there is a lack flexibility to explore such an approach with confidence.

While they were no doubt guided by the basic mechanisms of jet turbulence, it is important to recognize that most previous noise-reduction methodologies were not based on a detailed physical understanding of the noise sources. Historical noise reduction efforts leveraged the strong dependence of radiated noise amplitude on the jet exhaust velocity, being roughly U_j^8 (Lighthill 1952). More recent reductions in jet noise using nozzle geometry changes or by flow control are guided by hypotheses that have not been tested *a posteriori*. Frequently, these tests show that an increase in the high-frequency noise counters the gains achieved in the louder, low-frequency noise, and a favourable design might be viewed as the one that minimizes this high-frequency gain as well (Zaman, Bridges & Huff 2011). A more physics-based perspective is needed that could reduce the need for parametric testing, but turbulence has so far resisted a sufficiently simple mechanistic description.

Some recent efforts have pursued jet noise reduction based upon less empirical strategies. Maury *et al.* (2012) applied an automated procedure to minimize the high-frequency gain. Gudmundsson & Colonius (2007) and Koenig *et al.* (2013*b*) adopted wave-packet models to provide a physical description for noise reduction rather than

a simple empirical observation. It is hoped that the present results can both inform and perhaps provide an estimate of the ultimate potential of such methods.

Our approach to seeking a quieter state of otherwise similar jet turbulence uses adjoint-based optimization. It is formulated using \mathcal{H}^2 optimal control theory to determine an effective control. The need for a reduced mechanistic description of turbulence is avoided through direct integration of the large-eddy filtered equations of motion, following the PDE-based aerodynamic shape optimization of Jameson (1988, 1995). The adjoint of the perturbed and linearized Navier–Stokes equations is formulated so that its solution provides control sensitivity information that indicates a definite direction in which an incremental change in control forcing will reduce a particular metric of acoustic intensity. If a general actuator, such as we consider, can make the jet quieter by applying control as indicated by this direction, then we can conclude that it is feasible to perturb the jet with a simple actuation into a quieter state. However, it is also possible, given the complexity of jet turbulence and its generation of sound, that a quiet state might be relatively elusive, presenting a greater control challenge. Perturbations of control parameters can, in principle, also provide such conclusions. However, since the adjoint equation can be solved approximately at the same cost as the flow equation, the optimization procedure is far more tractable than a systematic parametric study.

The present study builds upon the work of Wei & Freund (2006) who first applied adjoint-based flow control for noise reduction to a two-dimensional subsonic mixing layer. In their study, the optimization algorithm demonstrated a significant 11 dB (92%) reduction in the sound cost functional defined on the lower-speed side of the mixing layer, and still showed a concomitant far-field noise reduction in all directions which, along with other analysis, showed that the noise suppression resulted from a manipulation of flow unsteadiness in a fashion that reduced its acoustic efficiency. The most effective reduction was obtained for a thermal controller modelled as a general heat source or sink. An analysis using the proper orthogonal decomposition suggested that the control renders the free shear flow quieter by making the convection of large-scale vortical structures more regular and thus similar to that of a harmonically excited free shear flow, which is less acoustically efficient. A subsequent study (Eschricht *et al.* 2007) confirmed that the sound sources in the context of Lighthill’s theory were weakened as a consequence of the noise reduction. Cavalieri *et al.* (2010) further showed that the noise reduction was associated with suppressing an intermittently large-amplitude, downstream-directed acoustic radiation. The physical phenomenon associated with the large-amplitude acoustic peaks was shown to be a triple vortex merging event. It is well understood, however, that the two-dimensional analogue of turbulence considered in those efforts is fundamentally different from actual jet turbulence. The flow in two dimensions is generally expected to be more organized and deterministic and therefore potentially more amenable to control. A goal of the present paper is to assess the viability of adjoint-based control to realistic jet turbulence. Given the optimal character of the the control we apply with a flexible actuation process, this study would help to provide an assessment of how controllable jet turbulence can be at nominal fixed flow conditions.

The flow conditions correspond to experimental data of Samimy *et al.* (2007), though we do not include the nozzle in our calculations. The governing equations and their adjoint are formulated in §2 to provide the necessary control sensitivity information needed to iteratively improve the noise-reducing control. High-fidelity, non-dissipative numerical techniques are integrated in a framework of large-eddy simulation and overset grid methodologies as discussed in §3. A realistic turbulent

jet, which reasonably matches the corresponding experimental measurements of both turbulence statistics and acoustics, is simulated at a moderate grid resolution, as discussed in §4. The adjoint-based formulation identifies a noise-reducing control in §5, where the near-field changes induced by the control are investigated to study noise-source mechanisms.

2. Optimal control formulation

The formulation is based upon that of aerodynamic shape optimization (Jameson 1988, 1995) extended for aeroacoustic control (Freund 2011). It is equivalent to that of Wei & Freund (2006) whose formulation followed more closely that of Bewley, Moin & Temam (2001) for incompressible turbulence control. More details are described elsewhere (Freund 2011).

The control \vec{F} and the cost functional \mathcal{J} to be reduced (the radiated sound in this study) have support only in an actuator region Γ and target region Ω , respectively. The cost functional $\mathcal{J} = \mathcal{J}(\vec{q}, \vec{F})$, in general, depends upon the time-dependent flow \vec{q} and the control \vec{F} such that the variation of \mathcal{J} is

$$\delta \mathcal{J} = \left(\frac{\partial \mathcal{J}}{\partial \vec{q}} \right)_{\vec{F}} \delta \vec{q} + \left(\frac{\partial \mathcal{J}}{\partial \vec{F}} \right)_{\vec{q}} \delta \vec{F}. \quad (2.1)$$

This relation, in principle, can be used to iteratively minimize \mathcal{J} ; however, it is unwieldy in practice since each $\delta \vec{F}$ corresponds to a new flow $\delta \vec{q}$, which would require a new flow simulation. The adjoint can be used to remove the dependence on $\delta \vec{q}$ so that the dependence of \mathcal{J} on $\delta \vec{F}$ can be directly utilized for a given \vec{q} . In the following, the optimal control formulation to do this is derived without direct reference to the details of the governing Navier–Stokes equations and their adjoint, which are discussed in §3.

We begin with the compressible Navier–Stokes equations written compactly as

$$\mathcal{N}(\vec{q}) = C(\mathbf{x})\mathbf{A}(\vec{q})\vec{F}, \quad (2.2)$$

where $C(\mathbf{x}) = 1$ for $\mathbf{x} \in \Gamma$ and 0 elsewhere to set the support of the control, and the 5×5 matrix \mathbf{A} is crafted to distribute the control \vec{F} appropriately within the \mathcal{N} system as shown below in (2.7). For notational simplicity, we define

$$\mathcal{M}(\vec{q}, \vec{F}) = \mathcal{N}(\vec{q}) - C(\mathbf{x})\mathbf{A}(\vec{q})\vec{F} = 0. \quad (2.3)$$

Upon introducing a Lagrange multiplier \mathbf{q}^\dagger and defining an inner product

$$\mathbf{a} \cdot \mathbf{b} = \int_{t_0}^{t_1} \int_{\mathbb{R}^3} \mathbf{a}^T \mathbf{b} \, dx \, dt, \quad (2.4)$$

(2.1) can be rewritten as

$$\delta \mathcal{J} = \left[\left(\frac{\partial \mathcal{J}}{\partial \vec{q}} \right)_{\vec{F}} - \mathbf{q}^\dagger \cdot \left(\frac{\partial \mathcal{M}}{\partial \vec{q}} \right)_{\vec{F}} \right] \delta \vec{q} + \left[\left(\frac{\partial \mathcal{J}}{\partial \vec{F}} \right)_{\vec{q}} - \mathbf{q}^\dagger \cdot \left(\frac{\partial \mathcal{M}}{\partial \vec{F}} \right)_{\vec{q}} \right] \delta \vec{F}, \quad (2.5)$$

where $\delta \mathcal{M} = 0$ was used in reflection of the fact that \vec{F} and \vec{q} satisfy the governing equation. If \mathbf{q}^\dagger is chosen such that the first term on the right-hand side is zero, $\delta \mathcal{J}$ can be directly related to $\delta \vec{F}$, independently of $\delta \vec{q}$. The $\delta \vec{q}$ term then does not have to be evaluated in (2.5), which makes the scheme viable for systems in which $\delta \vec{F}$ has

many degrees of freedom. Thus, \mathbf{q}^\dagger should solve

$$\mathbf{q}^\dagger \cdot \left(\frac{\partial \mathcal{M}}{\partial \vec{\mathbf{q}}} \right)_{\vec{\mathbf{F}}} \delta \vec{\mathbf{q}} = \left(\frac{\partial \mathcal{J}}{\partial \vec{\mathbf{q}}} \right)_{\vec{\mathbf{F}}} \delta \vec{\mathbf{q}}. \quad (2.6)$$

In the present study, \mathcal{N} represents the conserved form of compressible Navier–Stokes equations, which we express in terms of conserved variables $[\rho, \rho u, \rho v, \rho w, \rho E]^\top$, though for convenience the state vector $\vec{\mathbf{q}}$ is taken to be the primitive flow variables $[\rho, u, v, w, p]^\top$. Accordingly, the matrix \mathbf{A} in (2.2) is

$$\mathbf{A} = \begin{bmatrix} 1 & 0 & 0 & 0 & 0 \\ 0 & 1 & 0 & 0 & 0 \\ 0 & 0 & 1 & 0 & 0 \\ 0 & 0 & 0 & 1 & 0 \\ T_\infty/\gamma & u & v & w & 1 \end{bmatrix}, \quad (2.7)$$

where T_∞ is the ambient static temperature and $\gamma = C_p/C_v$ is a ratio of the specific heats. The adjoint field \mathbf{q}^\dagger is defined by $[\rho^\dagger, u^\dagger, v^\dagger, w^\dagger, p^\dagger]^\top$, although each adjoint variable does not necessarily carry a physical meaning in regard to the correspondingly named flow variable.

For aeroacoustic optimization, the most natural \mathcal{J} to be minimized is the integrated acoustic intensity over a target region Ω and some time interval $t_0 \leq t \leq t_1$:

$$\mathcal{J}(\vec{\mathbf{q}}, \vec{\mathbf{F}}) \equiv \int_{t_0}^{t_1} \mathcal{J}(t) dt \equiv \int_{t_0}^{t_1} \int_{\mathbb{R}^3} W(\mathbf{x}) [p(\mathbf{x}, t) - \bar{p}_0(\mathbf{x})]^2 d\mathbf{x} dt, \quad (2.8)$$

where $\bar{p}_0(\mathbf{x})$ is the time-averaged static pressure before any control is applied, and

$$W(\mathbf{x}) = \begin{cases} 1 & \text{for } \mathbf{x} \in \Omega \\ 0 & \text{for } \mathbf{x} \notin \Omega. \end{cases} \quad (2.9)$$

Note that the applied control is not penalized in \mathcal{J} .

With these choices, (2.6) is rewritten in more detail as

$$\begin{aligned} & \int_{t_0}^{t_1} \int_{\mathbb{R}^3} \delta \mathbf{q}^\top 2W(\mathbf{x}) [p(\mathbf{x}, t) - \bar{p}_0(\mathbf{x})] \left(\frac{\partial p}{\partial \mathbf{q}} \right)_{\mathbf{F}}^\top d\mathbf{x} dt \\ &= \int_{t_0}^{t_1} \int_{\mathbb{R}^3} \left\{ (\mathbf{q}^\dagger)^\top \left(\frac{\partial \mathcal{N}}{\partial \mathbf{q}} \right)_{\mathbf{F}} \delta \mathbf{q} - C(\mathbf{x}) (\mathbf{q}^\dagger)^\top \left(\frac{\partial \mathbf{A} \mathbf{F}}{\partial \mathbf{q}} \right)_{\mathbf{F}} \delta \mathbf{q} \right\} d\mathbf{x} dt. \end{aligned} \quad (2.10)$$

Integrating by parts, the right-hand side of (2.10) yields

$$- \int_{t_0}^{t_1} \int_{\mathbb{R}^3} \delta \mathbf{q}^\top \mathcal{N}^\dagger(\mathbf{q}^\dagger) d\mathbf{x} dt + b - \int_{t_0}^{t_1} \int_{\mathbb{R}^3} \delta \mathbf{q}^\top C(\mathbf{x}) \mathbf{A}^\dagger(\mathbf{q}^\dagger) \mathbf{F} d\mathbf{x} dt, \quad (2.11)$$

with the boundary contribution $b=0$ following the arguments of Wei & Freund (2006). With the matrix \mathbf{A}^\dagger defined as

$$\mathbf{A}^\dagger = \begin{bmatrix} 0 & 0 & 0 & 0 & 0 \\ 0 & p^\dagger & 0 & 0 & 0 \\ 0 & 0 & p^\dagger & 0 & 0 \\ 0 & 0 & 0 & p^\dagger & 0 \\ 0 & 0 & 0 & 0 & 0 \end{bmatrix}, \quad (2.12)$$

(2.10) reduces to

$$\mathcal{N}^\dagger(\mathbf{q}^\dagger) + C(\mathbf{x})\mathbf{A}^\dagger(\mathbf{q}^\dagger)\vec{\mathbf{F}} = -2W(\mathbf{x})[p(\mathbf{x}, t) - \bar{p}_0(\mathbf{x})] \left(\frac{\partial p}{\partial \vec{\mathbf{q}}} \right)_{\vec{\mathbf{F}}}^\top. \quad (2.13)$$

With \mathbf{q}^\dagger solving (2.13), the change in the cost functional from (2.5) can be further simplified for the aeroacoustic sound minimization as

$$\delta \mathcal{J} = C(\mathbf{x})\mathbf{q}^\dagger \cdot \mathbf{A}(\vec{\mathbf{q}})\delta\vec{\mathbf{F}}, \quad (2.14)$$

which provides the control sensitivity information. For the current control formulation, (2.14) is thus

$$\frac{\delta \mathcal{J}}{\delta \vec{\mathbf{F}}} = C(\mathbf{x}) \left[\rho^\dagger + \frac{T_\infty}{\gamma} p^\dagger, u^\dagger + up^\dagger, v^\dagger + vp^\dagger, w^\dagger + wp^\dagger, p^\dagger \right]. \quad (2.15)$$

Previous studies have demonstrated that a standard conjugate gradient algorithm along with Brent's line minimization (Press *et al.* 1986) provides reasonable convergence and was thus adopted in this study.

The adjoint equation parametrically depends upon the space–time resolved flow solutions. These fields were stored every 50 time steps at every mesh point, and linearly interpolated in time. Tests confirmed that the optimization process was insensitive to this (Wei 2004; Kim 2012).

3. Perfectly expanded Mach 1.3 jet simulation

3.1. Governing equations

In the present study, the unsteady, filtered Navier–Stokes equations for a compressible fluid were transformed to three-dimensional, generalized, curvilinear coordinates via a non-singular mapping $\mathbf{x} = X(\boldsymbol{\xi}, \tau)$ with inverse $\boldsymbol{\xi} = \Xi(\mathbf{x}, t)$. We employed the strong conservation form of Vinokur (1974) and Thomas & Lombard (1979). Upon introducing the Favre averaging,

$$\tilde{f} = \overline{\rho f} / \bar{\rho}, \quad (3.1)$$

where the overbar denotes the filtering operation, the governing equations solving for $\vec{\mathbf{Q}} = [\bar{\rho}, \bar{\rho}\tilde{u}_i, \bar{\rho}\tilde{E}]^\top$ are

$$\frac{\partial}{\partial \tau} \left(\frac{\bar{\rho}}{J} \right) + \frac{\partial}{\partial \xi_l} \left(\bar{\rho}\tilde{U}_l \right) = 0, \quad (3.2)$$

$$\frac{\partial}{\partial \tau} \left(\frac{\bar{\rho}\tilde{u}_i}{J} \right) + \frac{\partial}{\partial \xi_l} \left[\bar{\rho}\tilde{u}_i\tilde{U}_l + (\widehat{\xi}_l)_{x_i}\bar{p} \right] = \frac{1}{Re_\infty} \frac{\partial}{\partial \xi_l} \left[(\widehat{\xi}_l)_{x_j}(\tilde{\tau}_{ij} - \tau_{ij}^{SGS}) \right], \quad (3.3)$$

$$\begin{aligned} \frac{\partial}{\partial \tau} \left(\frac{\bar{\rho}\tilde{E}}{J} \right) + \frac{\partial}{\partial \xi_l} \left[(\bar{\rho}\tilde{E} + \bar{p})\tilde{U}_l - (\widehat{\xi}_l)_{i\bar{p}} \right] &= \frac{1}{Re_\infty} \frac{\partial}{\partial \xi_l} \left[(\widehat{\xi}_l)_{x_j}\tilde{u}_k\tilde{\tau}_{jk} \right] \\ &\quad - \frac{1}{Re_\infty Pr} \frac{\partial}{\partial \xi_l} \left[(\widehat{\xi}_l)_{x_j}(\tilde{q}_j + q_j^{SGS}) \right], \end{aligned} \quad (3.4)$$

$$\bar{p} = \frac{\gamma - 1}{\gamma} \bar{\rho}\tilde{T}, \quad (3.5)$$

with the normalized grid metrics defined by $(\widehat{\xi}_l)_{x_j} = J^{-1} (\partial \xi_l / \partial x_j)$ and the contravariant velocity in the ξ_l direction by $\tilde{U}_l = u_j(\widehat{\xi}_l)_{x_j} + (\widehat{\xi}_l)_l$. Reynolds and Prandtl numbers are

$Re_\infty = \rho_\infty c_\infty D / \mu_\infty$ and $Pr = \mu C_p / k = 0.72$, where D is the nozzle diameter and c is the isentropic speed of sound. A subscript ∞ indicates an ambient condition. The Reynolds number based on nozzle-exit conditions is $Re_D = \rho_j U_j D / \mu_j = 1.1 \times 10^6$. The resolved viscous stress tensor is

$$\tilde{\tau}_{ij} = J \frac{\tilde{\mu}}{Re_\infty} \left[\widehat{(\xi_k)}_{x_j} \frac{\partial \tilde{u}_i}{\partial \xi_k} + \widehat{(\xi_k)}_{x_i} \frac{\partial \tilde{u}_j}{\partial \xi_k} \right] + J \frac{\tilde{\lambda}}{Re_\infty} \widehat{(\xi_l)}_{x_k} \frac{\partial \tilde{u}_k}{\partial \xi_l} \delta_{ij}, \quad (3.6)$$

and the resolved heat flux is

$$\tilde{q}_j = -J \frac{\tilde{\mu}}{Re_\infty Pr} \widehat{(\xi_k)}_{x_j} \frac{\partial \tilde{T}}{\partial \xi_k}. \quad (3.7)$$

The temperature-dependent viscosity is

$$\tilde{\mu} = \left[(\gamma - 1) \tilde{T} \right]^n, \quad (3.8)$$

with $n = 0.666$ modelling air (Thompson 1991). The second coefficient of viscosity $\tilde{\lambda}$ is related to the resolved bulk viscosity $\tilde{\mu}_B$ via $\tilde{\lambda} = \tilde{\mu}_B - (2/3)\tilde{\mu}$ with $\tilde{\mu}_B = 0.6\tilde{\mu}$ chosen as a model for air (Thompson 1991).

The terms labelled by the superscript *SGS* in (3.3) and (3.4) indicate the subgrid-scale stress and heat flux. These were modelled by a standard dynamic Smagorinsky model formulated for a compressible fluid (Moin *et al.* 1991) with Lilly's improvement (Lilly 1992). The implementation is similar with that of Rizzetta, Visbal & Blaisdell (2003). A fifteen-point wavenumber-optimized filter (Bogey & Bailly 2004) was applied to determine the subtest-scale dissipation. The subgrid-scale model coefficients were averaged in the azimuthal coordinate.

3.2. Discretization

A thirteen-point, fourth-order, centred, explicit coefficient-optimized finite-difference scheme (Bogey & Bailly 2004) was used to evaluate first derivatives in space. Near boundaries, a seven-point boundary closure of Berland *et al.* (2007) was applied. The second derivatives in the viscous fluxes are approximated by repeated first derivatives.

For large-eddy simulation, such low-dissipation schemes often require weak filtering to remain stable. For this, we employed an eleven-point, implicit Padé filter (Lele 1992; Gaitonde & Visbal 1998) with the free parameter $\alpha_f = 0.47$. Both forward and adjoint solutions were filtered at every time step in every direction in the computational coordinates.

A standard four-stage Runge–Kutta method time advanced flow and adjoint solutions with time step $\Delta t c_\infty / D = 0.0009$, which corresponded to a CFL number of approximately 0.5.

Physical boundaries were modelled with one-dimensional characteristic boundary conditions (Poinsot & Lele 1992) formulated in generalized coordinates (Kim & Lee 2000) for both the Navier–Stokes equations and their adjoint. Their details are described elsewhere (Kim 2012). To further reduce unphysical reflections, an additional zone with a damping term (Freund 1997; Bodony 2006) was added to the right-hand side of (3.2)–(3.4):

$$-\frac{\Upsilon(\mathbf{Q} - \mathbf{Q}_{ref})}{J}, \quad (3.9)$$

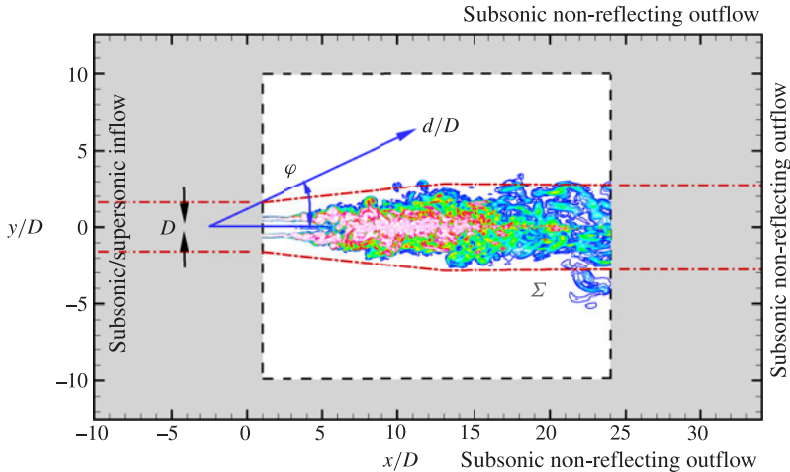


FIGURE 1. (Colour online) Computational domain on the x - y plane. The shaded zone is an absorbing buffer region and Σ indicates the Ffowcs Williams and Hawkins surface.

where

$$\Upsilon = 0.5 \left(\frac{|\mathbf{x} - \mathbf{x}_0|}{|\mathbf{x}_b - \mathbf{x}_0|} \right)^2, \quad (3.10)$$

so that the damping increases its strength from $\mathbf{x} = \mathbf{x}_0$ until it reaches its maximum at $\mathbf{x} = \mathbf{x}_b$. The reference solution \mathbf{Q}_{ref} is discussed in the next section. The same parameters were used for the adjoint Navier–Stokes simulations; however, since the adjoint Navier–Stokes equations are integrated backward in time, the sign of Υ is changed (Wei 2004).

3.3. Simulation details

A schematic of the computational domain is shown in figure 1. A cylindrical coordinate system was employed with radial, azimuthal and streamwise variables (r, θ, x) , with $r = 0$ along the jet axis and $x = 0$ the nozzle-exit plane. Also shown in figure 1 are a distance d to a far-field location at a polar angle ϕ . The solutions on overset-grid block interfaces were interpolated by interpolation stencils generated at the pre-processing stage by PEGASUS (Suhs, Rogers & Dietz 2002) and BELLERO (Sherer, Visbal & Galbraith 2006). To keep the computational cost manageable for the optimization, it was decided to neglect the nozzle geometry in the simulation, as has been done successfully in previous simulations (Freund 2001; Bogey, Bailly & Juvé 2003; Uzun, Lyrantzis & Blaisdell 2004; Bodony & Lele 2005).

The simulation domain was discretized by two overset-grid blocks. A Cartesian grid was used near $r = 0$ while the rest of the simulation domain was discretized by a cylindrical grid. The domain size was $12.5D$ in the radial direction and $34D$ in the axial direction. The absorbing buffer zone extended outward from $r/D = 10$ in the radial direction and was active for $x/D < 1$ and $x/D > 24$ in the axial direction, as shown in figure 1. The Cartesian grid had $451 \times 21 \times 21$ points in streamwise, vertical, and spanwise directions, respectively, and the cylindrical grid had $184 \times 32 \times 451$ points in the radial, azimuthal and streamwise directions, respectively. The total number of grid points was thus $\sim 2.9 \times 10^6$.

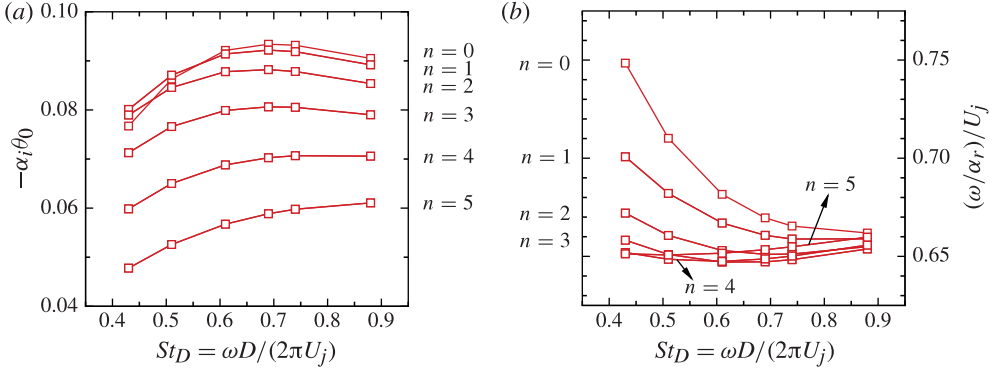


FIGURE 2. (Colour online) Dispersion relations of instability waves. The streamwise wavenumber is $\alpha = \alpha_r + i\alpha_i$ and θ_0 is the momentum thickness. (a) Streamwise growth rate of each instability mode and (b) phase speed of each instability mode.

3.4. Inflow data

Since the nozzle was not explicitly included, a realistic inflow was imposed based upon a separate Reynolds-averaged Navier–Stokes (RANS) simulation for the converging–diverging nozzle of the corresponding experiment (Samimy *et al.* 2007). The converged RANS solution was interpolated to provide the mean inflow data as well as the initial condition and the reference solution \mathbf{Q}_{ref} for the absorbing buffer zone in (3.9). However, a steady inflow tends to remain laminar artificially far downstream. Thus, we added small-amplitude, parallel-flow, instability modes $\mathbf{q}'(\mathbf{x}, t) = \hat{\mathbf{q}}(r) \exp[i(\alpha x + n\theta - \omega t + \phi)]$ to facilitate realistic transition. The phase difference ϕ was adjusted by a random-walk process to disrupt the exact periodicity (Lui 2003). The dispersion relations of the instability waves are shown in figure 2(a,b). The jet column mode frequency $St_D \approx 0.3$ was not included since it is known to generate large-scale organized vortical structures (Crow & Champagne 1971) that are qualitatively different from the laboratory observations (Samimy *et al.* 2007). Overall sixty modes were excited: six discrete frequencies $St_D = 0.43, 0.51, 0.61, 0.69, 0.74$, and 0.88 were chosen for azimuthal mode numbers $n = \pm 1, \pm 2, \dots, \pm 5$. The axisymmetric ($n = 0$) mode was not included. We shall see in §5 that $n = 0$ is particularly important in the effect of the control, and it is therefore noteworthy that it was not directly excited at the inflow. The total magnitude of the inflow excitation was set to induce a maximum root-mean-squared (r.m.s.) streamwise inflow velocity fluctuation of $0.03U_j$.

3.5. Far-field sound

Sound beyond the computational domain was calculated using a Ffowcs Williams and Hawkins surface (Ffowcs Williams & Hawkins 1969) in an advanced time formulation (Casalino 2003). A mesh-aligned, approximately cylindrical surface with open ends was used (see figure 1). Its radius was $1.6D$ at the inflow and $2.8D$ at the outflow. On this surface, the maximum resolved frequency was estimated, using the resolutions of the finite-difference scheme and the surface grid, to range between $St_{D,max} \approx 1.0$ and ≈ 1.5 , depending on the far-field angle. The maximum r.m.s. fluctuation of vorticity magnitude on the surface $(\overline{\omega'_i \omega'_i})^{1/2} / |\partial \bar{u}_x / \partial r|_{max}$ was less than 0.03. Moving the integral surface farther from the jet than shown in figure 1

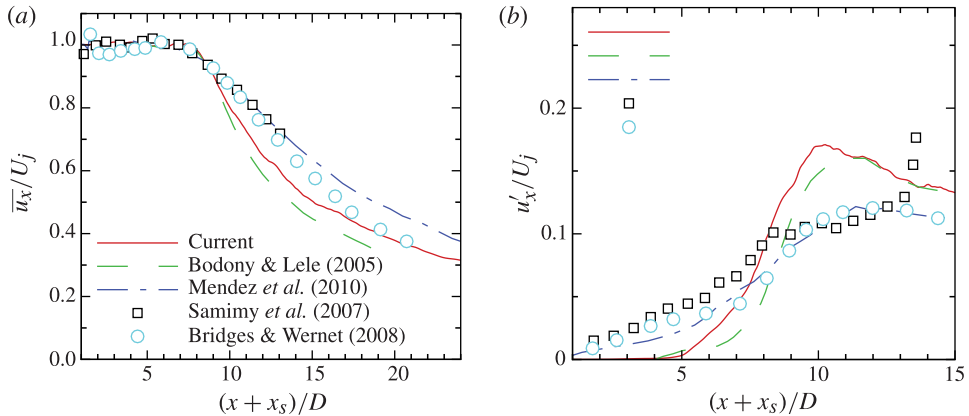


FIGURE 3. (Colour online) Comparison of centreline turbulence statistics: (a) time-averaged streamwise velocity and (b) streamwise velocity r.m.s. fluctuations, where $x_s/D = 2.3$ for the current simulation, and 4.0 for Bodony & Lele (2005).

reduced sound levels mainly at higher frequencies, presumably due to the decreased maximum $St_{D,max}$ that can be resolved on the integral surface (Uzun *et al.* 2004). Detailed validation is provided elsewhere (Kim 2012).

4. Uncontrolled jet turbulence and sound radiation

The uncontrolled baseline Mach 1.3 jet was simulated until it reached a statistically stationary state before statistics were collected. Here, we describe the main features of its turbulence and radiated sound; additional details are reported elsewhere (Kim 2012). Centreline statistics are compared with experimental and other numerical data for similar jet conditions in figure 3(a,b). Since we did not include a nozzle in our calculations, the streamwise coordinate was shifted so that the potential core length, defined by the axial location where the mean streamwise velocity is $0.95U_j$, matched the measurement of the most closely corresponding experiment (Samimy *et al.* 2007). The current simulated jet spreads somewhat more rapidly compared with the laboratory jet experiments (Samimy *et al.* 2007; Bridges & Wernet 2008) and the simulation of Mendez *et al.* (2010), where six times more mesh points were used with the nozzle explicitly included. Its decay rate is closer to the Mach 0.9 turbulent jet simulation without a nozzle using the same inflow excitation and comparable grid resolution (Bodony & Lele 2005). The growth and decay pattern of the streamwise turbulence intensity observed in figure 3(b) is typical of other simulations without a nozzle (Bodony & Lele 2005; Bogey & Bailly 2006).

Spectra of radial velocity fluctuations are compared with jets at similar flow conditions in figure 4. Despite the somewhat different flow conditions, the current simulated jet has a realistic broad-banded turbulence spectrum without distinct frequency peaks in agreement with the other reported results. Also, this comparison suggests that the current spatial resolution would be sufficient to resolve frequencies up to $St \approx 5$ in the turbulence.

Far-field sound spectra at $\varphi = 30^\circ$ and 90° are shown in figure 5(a,b). Agreement at $\varphi = 30^\circ$ is within 0.5 dB up to $St_D \approx 1.5$, where it falls off as expected due to the finite resolution of the simulation. At $\varphi = 90^\circ$, the spectrum deviates from the experimental measurement at a lower $St_D \approx 0.7$.

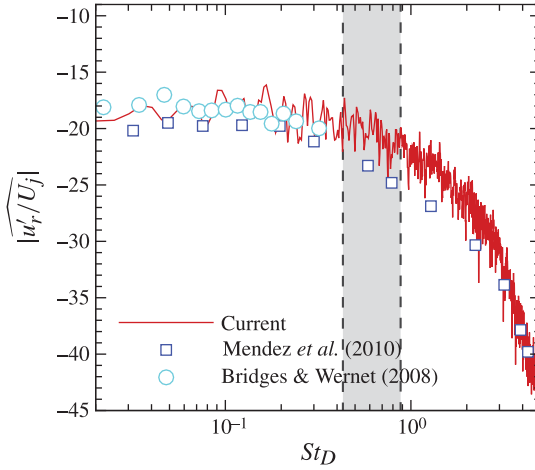


FIGURE 4. (Colour online) Power spectral density of radial velocity fluctuation at $x/D = 8$, $r/D = 0.5$. The shading indicates the range of St_D excited at the inflow. The symbols show the Mach 1.4 heated jet data of Bridges & Wernet (2008) and Mendez *et al.* (2010) at the same location relative to the end of the potential core ($x/D = 10$, $r/D = 0.5$).

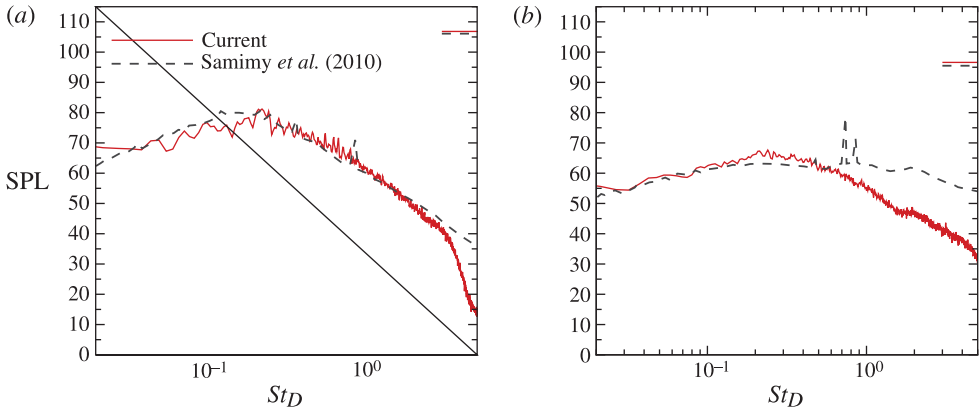


FIGURE 5. (Colour online) Sound pressure level measured at (a) $d/D = 94$ and $\varphi = 30^\circ$, and (b) $d/D = 44$ and $\varphi = 90^\circ$. Spectra were projected to a common distance $80D$. Line segments at the upper-right corner indicate overall sound pressure level (OASPL).

The acoustic directivity is shown in figure 6. The sound calculation was made at $d/D = 72$, and other measurement data were scaled to that location. Due to the slight difference in the nozzle-exit velocity U_j , a U_j^8 scaling was applied. The current data agree most closely with the Mach 1.3 cold jet of Hileman (2004). There is a small but nearly uniform over-prediction compared with the Mach 1.4 cold jet noise measurement of Tanna (1977), which is also similar to the $M_j = 1.4$ data of Bridges & Wernet (2008).

5. Noise-reduced Mach 1.3 jet

5.1. Control configuration

The Mach 1.3 jet discussed in §4 provides the baseline for our study of noise reduction. The results showed that the jet turbulence is realistically broad-banded and

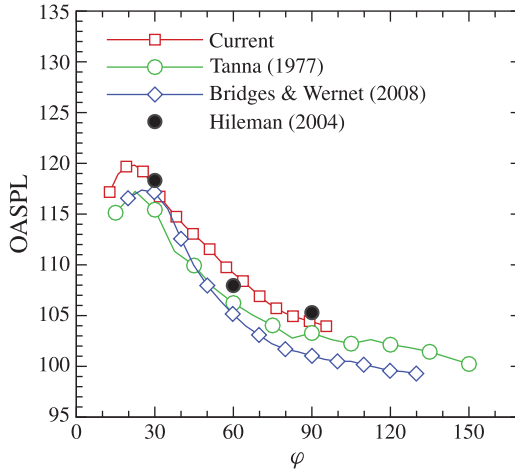


FIGURE 6. (Colour online) The sound directivity at $d/D=72$. A U_j^8 scaling was applied to compare the $M_j = 1.4$ data of Tanna (1977), the $M_j = 1.4$ data of Bridges & Wernet (2008), and the Mach 1.3 data of Hileman (2004) with the present Mach 1.3 result.

produces a similarly broad-banded acoustic field that agrees well with the experimental data, especially at low angles to the jet axis, where the sound is most intense. In figure 7, the optimization procedure is shown schematically. The control \vec{F} , which has support in Γ , was adjusted to reduce the aeroacoustic cost functional \mathcal{J} , measured on the control target Ω . The control was a thermal source in the compressible Navier–Stokes equations and modelled heat-release effects from an actuator located near the nozzle exit, inspired in part by arc-filament plasma actuators (Samimy *et al.* 2007). The actuator region was a ring-shaped volume within $0.3 \leq r/D \leq 0.7$ and $1.0 \leq x/D \leq 3.0$ that encompassed the initial jet shear layer. Clearly, this actuation does not correspond directly to any particular hardware; it was designed as a model for a localized actuation near the nozzle lip for assessing the effectiveness of the current control algorithm for the potential of near-nozzle actuation for noise reduction. The target surface Ω was a cylindrical surface located at $r/D = 8$ and spanned the entire streamwise physical domain. The control time horizon was $\mathcal{T} = 90$, long enough to include more than 20 jet column mode periods (Crow & Champagne 1971). Figure 8 shows the instantaneous cost functional \mathcal{J} of the uncontrolled jet over the entire simulated time period of approximately 27 flow-through times. The period \mathcal{T} corresponds to the control time interval.

There was no constraint on the space and time profiles of the control and thus all space–time points in Γ over \mathcal{T} were independently optimized. This includes $\sim 140 \times 10^3$ mesh points over 2×10^3 time steps, so the total number of parameters to be optimized was approximately 280×10^6 .

5.2. Noise reduction

5.2.1. Cost functional

Figure 9(a) shows how the sound cost functional \mathcal{J} defined by (2.8) was reduced after three conjugate gradient iterations. We conjecture that further line searches could yield additional noise reduction, though our goal is to study the reduction, not to

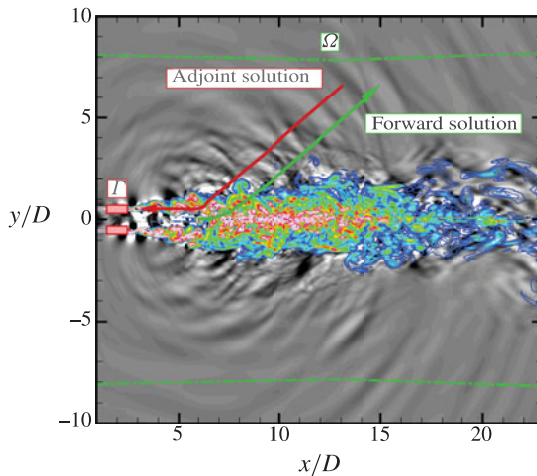


FIGURE 7. (Colour online) A schematic of adjoint-based control of the Mach 1.3 jet with the actuator Γ and the target Ω regions. Vorticity magnitude is shown with contours (maximum $|\omega| = 6$) and the grey-scale flood levels show the acoustic field with divergence of velocity between -0.03 and 0.03 .

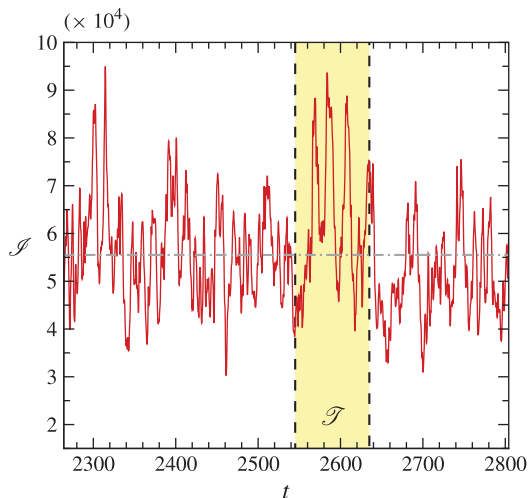


FIGURE 8. (Colour online) Instantaneous cost functional \mathcal{J} of the uncontrolled jet. The dashed-dot line indicates the time-averaged acoustic intensity. The period \mathcal{T} corresponds to the control time interval.

identify a minimum, since it would surely depend upon the actuator design. This objective also motivated our choice of such a general actuator in §5.1. Overall, a 16.3% reduction was obtained with respect to the initial \mathcal{J} .

Figure 9(b) shows the change in the corresponding instantaneous cost functional \mathcal{J} defined in (2.8). Hereafter, t represents time since the optimization begins: $t \triangleq t - t_0$. The uncontrolled jet shows particularly strong acoustic energy radiation, more than twice the acoustic energy that the jet radiated in its relatively quiet periods. The

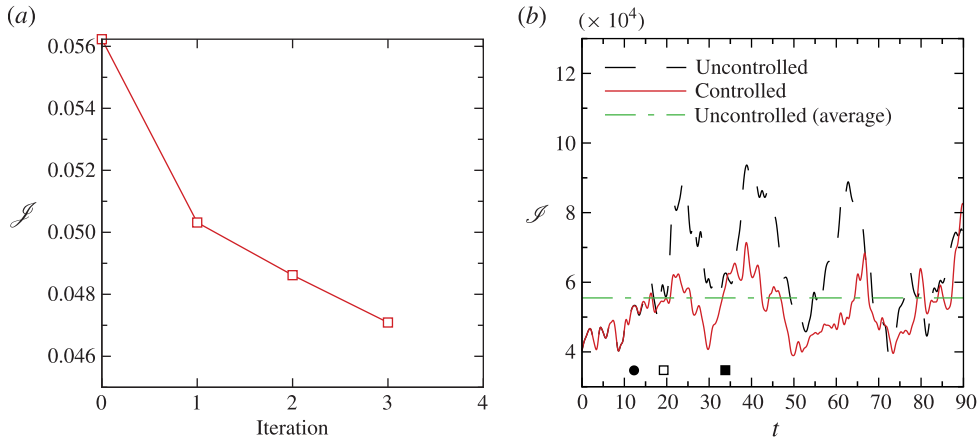


FIGURE 9. (Colour online) (a) The reduction of the cost functional \mathcal{J} . (b) Instantaneous cost functional defined in (2.8) over the control horizon. The circle is the estimated control onset and the squares are the minimum and maximum estimated control onset (see the text), respectively, based upon flow-convective and acoustic propagation time of the energetic control events $C_{1,2,3}$ discussed in §5.3.

control reduced noise via suppressing the large-amplitude peaks below the average level of acoustic intensity that the uncontrolled jet radiated.

As discussed by Wei & Freund (2006), the sound cannot be immediately reduced starting from $t=0$. This delay can be estimated based upon the instability convection speed $U_c/U_j \approx 0.66$ shown in figure 2(b) and the potential core length, $L_c/D \approx 6.17$. Thus, the convective time to the end of the potential core plus acoustic propagation time to the target surface would anticipate a control-effect onset at $t=12.3$, which is denoted by the circle in figure 9(b). Calculating reduction only after this delay, the noise reduction is 18%.

To better quantify the characteristics of the noise reduction, the pressure fluctuations on the target surface Ω were decomposed into their azimuthal components. Figure 10(a) shows that, close to the jet axis, the axisymmetric component ($n=0$) of the sound was most suppressed, followed by the first helical component ($n=1$). At angles further from the downstream axis, the sound reduction is smaller, as seen in figure 10(b), and unevenly distributed amongst the azimuthal Fourier modes $n \leq 5$. For all radiation angles, changes are negligible for $n \gtrsim 5$. Figures 11(a) and 11(b) show the instantaneous axisymmetric component of the sound at $\varphi = 20^\circ$ and 50° . At $\varphi = 20^\circ$, a series of large-amplitude acoustic peaks are suppressed, which also shows clearly that the $\mathcal{J}(t)$ peaks in figure 9(b) include the combined effect of several intense sound waves. The control effects at the higher angle are relatively insignificant. These observations demonstrate that the current jet had a period during which it radiated a series of particularly strong sound waves, primarily axisymmetric in θ and primarily downstream, and the control suppressed them significantly. Several previous studies reported similar particularly loud, intermittent sound radiation from axisymmetric jets (Juvé, Sunyach & Comte-Bellot 1980; Hileman & Samimy 2001; Bogey *et al.* 2003; Hileman *et al.* 2005; Kastner *et al.* 2006; Cavalieri *et al.* 2011a,b; Kerhervé *et al.* 2012; Koenig *et al.* 2013a).

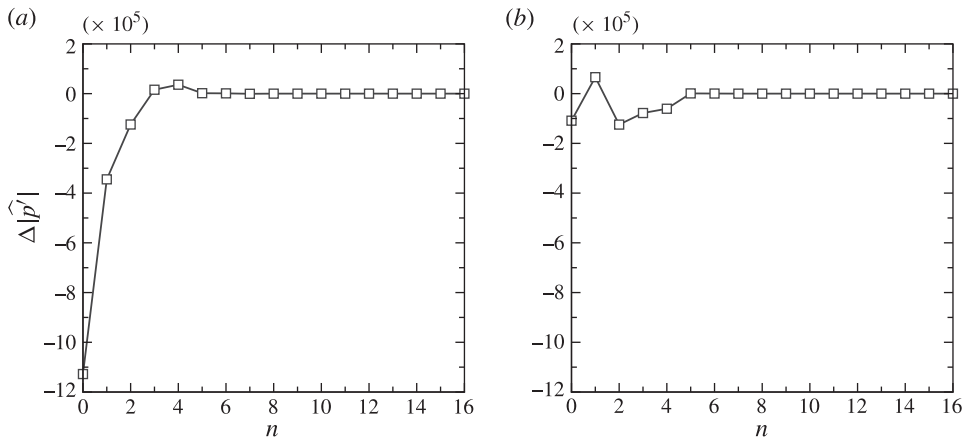


FIGURE 10. Azimuthal amplitude changes of sound on the control target surface Ω : (a) $\varphi = 20^\circ$; (b) $\varphi = 50^\circ$.

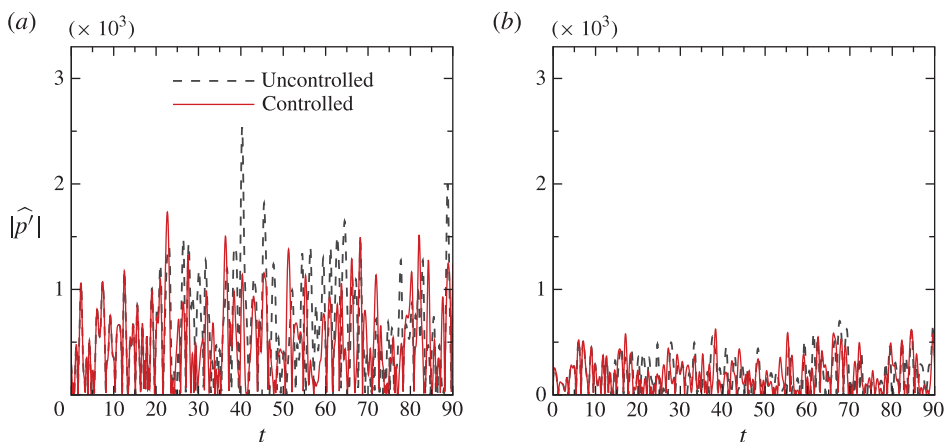


FIGURE 11. (Colour online) Instantaneous axisymmetric sound amplitudes on the control target surface Ω : (a) $\varphi = 20^\circ$; (b) $\varphi = 50^\circ$.

5.2.2. Far-field sound

Though it was not directly targeted by the control, the far-field acoustic radiation was also reduced. Acoustic spectra calculated at $d/D = 80$ are shown in figure 12(a,b) before and after the control was applied. At $\varphi = 30^\circ$, most of the noise reduction is for $0.1 \leq St_D \leq 0.4$, which includes the jet preferred frequency (Crow & Champagne 1971). The maximum reduction in SPL at $\varphi = 30^\circ$ is 5 dB at $St_D = 0.2$. The predominant influence of the control at low frequencies and downstream angle can be anticipated, since these make by far the greatest contribution to \mathcal{J} . The formulation is such that the control effort is naturally biased toward the loudest part of the noise because, given equal degrees of controllability, that provides the steepest gradient. In this regard, studying cost functionals weighted to target particular directions or spectral components would be an interesting generalization of our formulation. It is

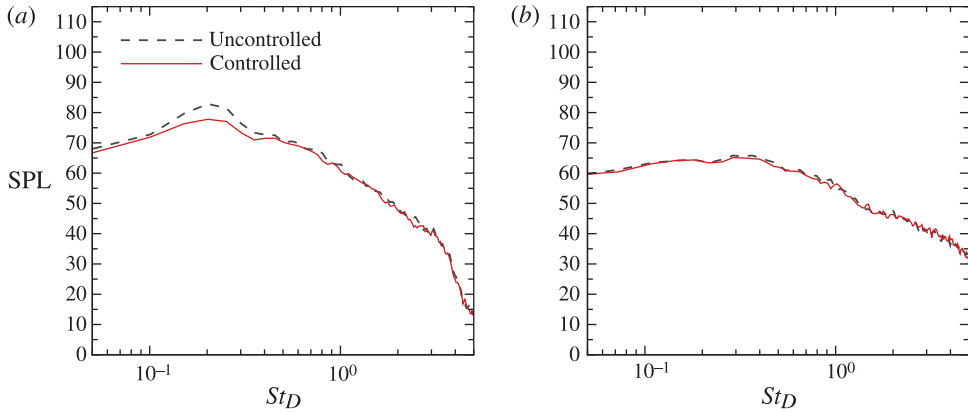


FIGURE 12. (Colour online) Sound pressure level measured at (a) $d/D=94$ and $\varphi=30^\circ$, and (b) $d/D=44$ and $\varphi=90^\circ$. Spectra were projected to a common distance $80D$.

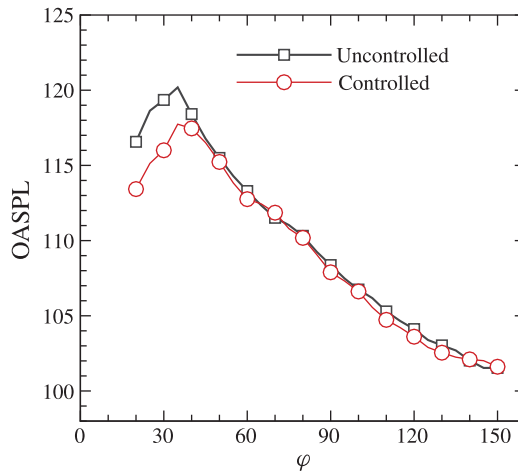


FIGURE 13. (Colour online) The sound directivity change at $d/D=72$.

noteworthy that in contrast to many control efforts (e.g. Samimy *et al.* 2010; Zaman *et al.* 2011), the high-frequency noise radiated to 90° was not increased.

The modification of sound directivity in figure 13 shows that OASPL is reduced at almost every angle, with its maximum reduction of 3.5 dB at $\varphi=25^\circ$. Most of the sound reduction occurs for $\varphi \lesssim 40^\circ$. Also, the suppressed noise sources radiated primarily at lower radiation angles for the frequency range of $0.1 \leq St_D \leq 0.4$, which, together with the axisymmetric dominance in noise reduction in figure 10(a), suggests that the current noise sources of particularly intense radiation originated from the motions of large-scale structures (Jordan & Colonius 2013).

5.3. Noise-reducing control

5.3.1. Space–time structure of the control

Figure 14(a,b) shows the space–time distribution of the control at $x/D=1.5$ on the nozzle lipline $r/D=0.5$, where the control forcing was most energetic. In figure 14(a),

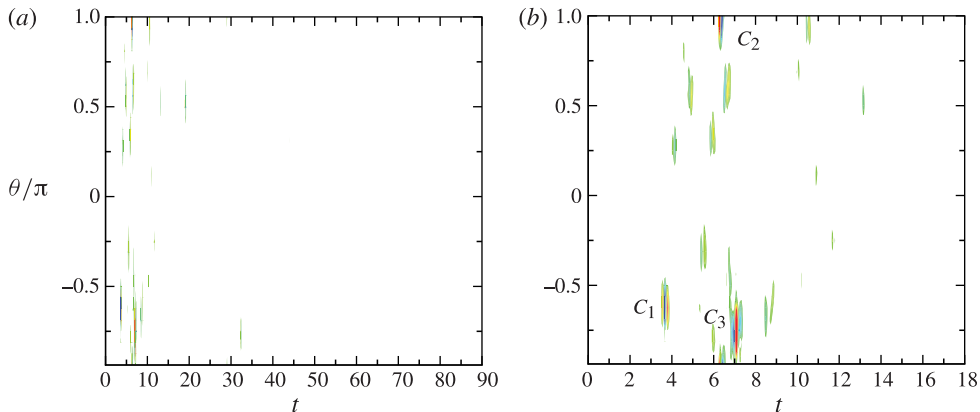


FIGURE 14. (Colour online) The space–time contours of the control F at $x/D = 1.5$ and at the lipline: (a) over the entire control horizon and (b) over the time period of 18.

we see that the control is particularly strong for only the initial 30% of the full control interval, after which its magnitude becomes relatively small. Especially energetic control events are concentrated within $t < 10$. The same travel-time arguments as for the controls effects (e.g. in regard to figure 9b) apply to the adjoint, which has the same characteristic speeds of the flow equations; however, we expect only the final 12.3 time to be without finite control in this case. Figure 14(b) shows a magnified view of figure 14(a) for the initial 20% of the control horizon. During this period, the control events appear as distinct and distributed events in θ and in t , without obvious organization. Among them, three particularly strong control events are designated C_1 , C_2 and C_3 . This clustering near $t = 0$ is surprising since the sound was reduced for most of \mathcal{T} as seen in figures 9(b) and 11(a). The streamwise evolution of these events within the control region reflects the advection of the turbulence structures with slowly decreasing control amplitude downstream. Figure 15, for example, shows the x – t behaviour of the $n = 1$ azimuthal Fourier mode. Other components show the same behaviour.

Assuming that a series of near-field events constitute a sound source that persists throughout the time horizon considered, these results suggest that the control suppressed their collective onset rather than acting to somehow counteract individual loud events. This is counter to the expectation based upon the convective velocity of turbulence, since taken from this perspective the control would target each loud event separately. In figure 9(b), the locations of the square symbols represent the minimum and the maximum estimated times, based upon convective speeds and sound propagation times, at which the perturbed sound radiation by the major control events C_1 and C_3 can reach Ω . The acoustic radiation seems to start to respond when the perturbed sound radiation of the jet induced by C_1 reaches Ω . Simple travel-time arguments suggest that direct control influence on the sound radiation lasts only for the period corresponding to the first acoustic peak in figure 9(b), though significant noise reduction continues for the remainder of the control time horizon. In figure 14(a), we see that there are control events for $10 \leq t \leq 35$, though they are lower energy and less frequent. We investigate this in the next section.

It is interesting to note the range of time scales that we see when we consider the sound and its control. The control events are spaced by $\Delta t \approx 2.5$, which would

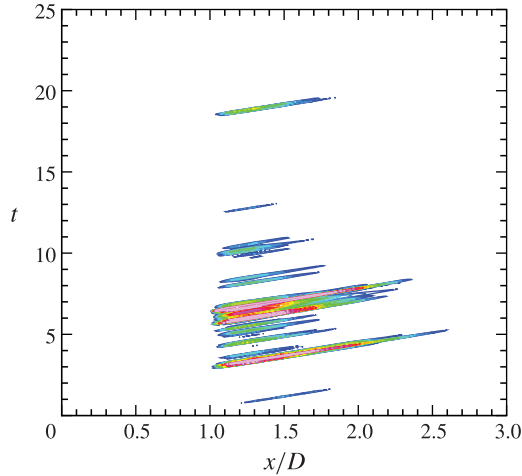


FIGURE 15. (Colour online) The instantaneous $n=1$ azimuthal amplitude of the control at the lipline.

correspond to $St \approx 0.4$, which is about the column mode frequency of most jets. However, significant control events seem to suppress sound over a period that would correspond to $St \approx 0.02$ as shown in figure 12(a). This mismatch is particularly intriguing since the long-time scale also corresponds to the length of the especially loud sound events noted in figure 9(b). A possible interpretation is that a burst of control over a short period can move the jet into an extended period of relative quiet, which seems to be self-sustaining. A quantitative description of this is, however, tied up in the challenge of describing the sound generation processes in the first place, as discussed in §1, and thus for now at least this perspective will remain speculative.

5.3.2. Selective application of the control

We can test the apparent dominance and persistent effect of early energetic control events by selectively applying them only early in the simulated time horizon. If $C_{1,2,3}$ are indeed dominant with respect to the observed noise reduction, there should be nearly the same reduction of \mathcal{J} when the control is only applied up to the time of event C_3 .

Figure 16(a–c) shows the effect of turning off the control at $t=10$, 20 and 30, all of which are after the C_3 event. When the control is turned off at $t=10$ in figure 16(a), the noise reduction appears to be ineffective for later times. So, despite the intensity of $C_{1,2,3}$, the noise reduction was not due to them alone, though the noise reduction was still 9.6%, approximately half of the original noise reduction of 19%. This is significant but disproportionately large, as might be expected based upon figure 14.

In figure 16(b), the control is terminated at $t=20$ and the cost functional closely follows that of the fully controlled jet until $t \approx 34$ (see the solid dot). While the cost functional does respond to the change of the control as strongly, the noise reduction continues up to $t \approx 55$. Hence, figure 16(b) shows that additional control events in $10 \leq t \leq 20$ do act to suppress the first and the second large-amplitude peaks. Considering figure 11(a), each of the $\mathcal{J}(t)$ events corresponds to several sound waves. The overall noise reduction was 15.2%, close to the original noise reduction of 19%.

Interestingly, the control shut down at $t=30$ only achieved 15.6%, as shown in figure 16(c), almost indistinguishable from the $t=20$ result in figure 16(b). This shows

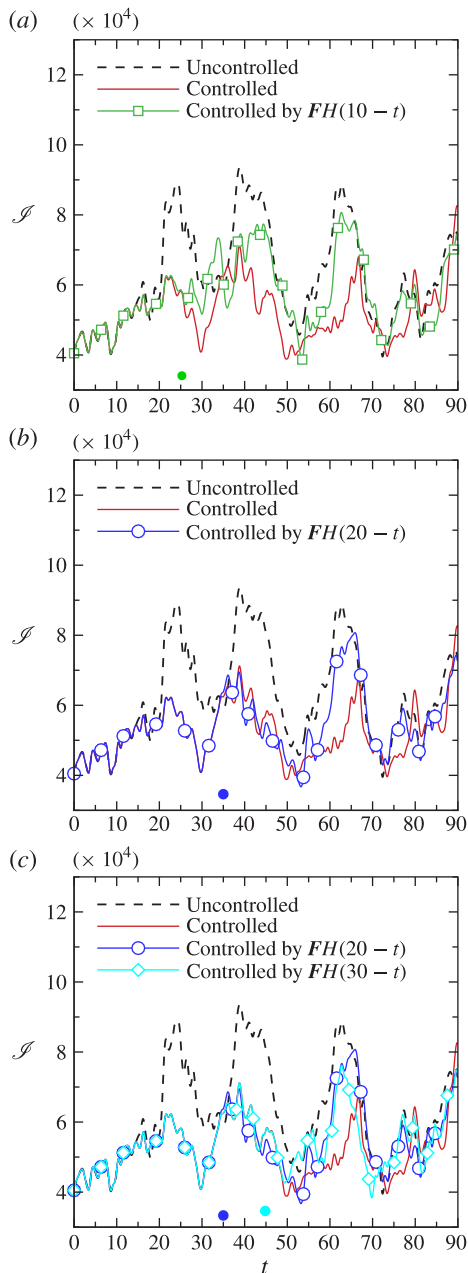


FIGURE 16. (Colour online) Instantaneous cost functionals when the control was turned off after (a) $t = 10$, (b) $t = 20$, and (c) $t = 30$. $H(t)$ denotes the Heaviside function. The solid circle in each figure represents the estimated influence time on Ω corresponding to when the control was turned off.

that any control events occurring between $t = 20$ and 30 would have little impact on the acoustically loud events. The observation that the third large-amplitude peak was only slightly influenced by switching off the control in this way implies that the acoustically loud events for $55 \leq t \leq 70$ may have a different origin to those suppressed

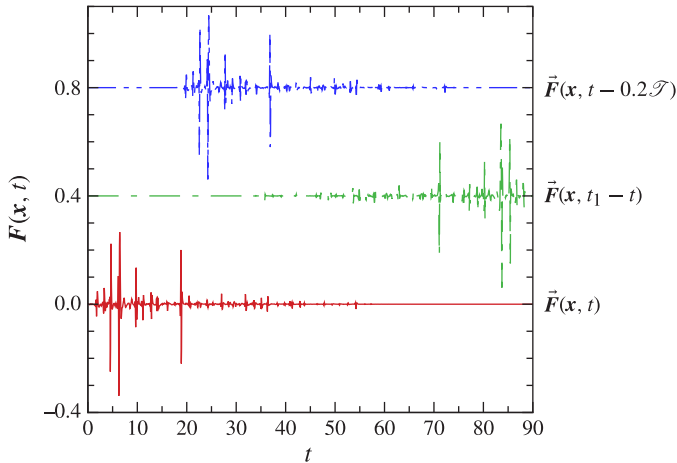


FIGURE 17. (Colour online) Time history of the applied control at $x/D = 1.3$ and $r/D = 0.5$. Non-solid lines were shifted by 0.4 along the vertical axis.

at earlier times. However, the earlier acoustically loud events do not appear to be completely independent since there is some reduction for $55 \leq t \leq 70$ in figure 16(c).

Collectively, these tests demonstrate that the control events up to $t = 20$ lead to the noise reduction up to $t \approx 55$. Considering that the longest propagation time delay to Ω was 15 for $\varphi = 20^\circ$, the noise reduction cannot be completely explained by a simple control event plus advection time; rather, the control effects persisted for a longer time period, without a one-to-one correspondence between control events and acoustic events.

5.3.3. Phase relation between the control and the jet

Though the control effect seems to persist longer than expected based upon convective time scales, we can anticipate that its effectiveness still must depend upon its correlation with the turbulence. To assess this, we consider the changes in \mathcal{J} when the same noise-reducing control $\vec{F}(\mathbf{x}, t)$ was applied differently from the precise time of its optimization: backward in time $\vec{F}(\mathbf{x}, t_1 - t)$ and delayed by 20% of the control horizon $\vec{F}(\mathbf{x}, t - 0.2\mathcal{T})$, as shown in figure 17. Over the entire control horizon, the control applied backward in time increases \mathcal{J} by 0.06% (figure 18a), while the 20%-delayed actuation achieves only a 2.3% reduction (figure 18b). We conclude that, indeed, the control worked in conjunction with the turbulence structures and perhaps the natural instabilities of the jet to suppress its acoustic efficiency. Note also that, were a linear acoustic cancellation rather than a more subtle manipulation of the jet turbulence the control mechanism, this exercise would be expected to increase sound.

5.4. Visualization of the controlled turbulence

Given the relation between the control and the time-dependent flow, we attempt to identify structural changes associated with noise suppression. Figure 19(a–d) shows the development of the azimuthal vorticity ω_θ at $\theta/\pi = -3/4$, corresponding to the approximate azimuthal location of C_3 in figure 14(b). The horizontal axis in these figures was transformed to provide the perspective of an observer moving at

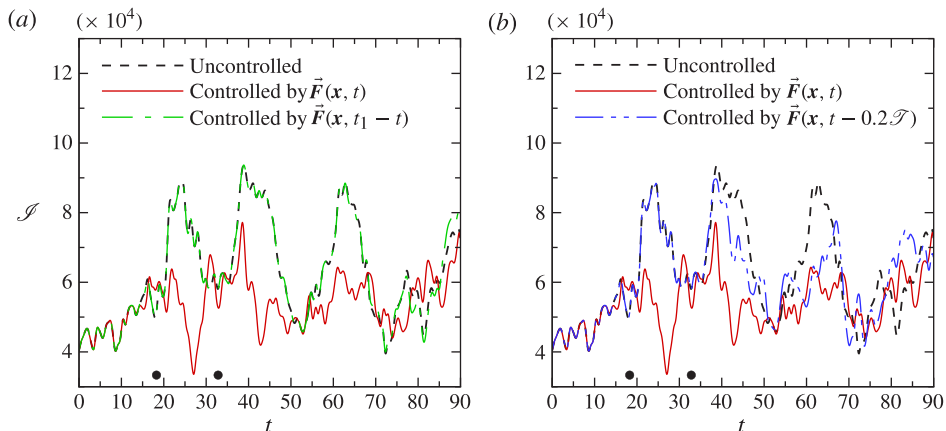


FIGURE 18. (Colour online) Instantaneous cost functionals when a control of different phase was applied for the second line search.

the convective velocity, $U_c/U_j = 0.66$. In figure 19(a), the uncontrolled-jet shear layer shows a reduced growth in time in the period between 6 and 10, marked by the shaded region. In contrast, the control seems to spawn new small rolled-up structures (marked by arrows). Further downstream, the development of the shear layer shown in figure 19(b–d) becomes more complicated. However, the interaction in the circled regions of figure 19(c) is more distributed in the controlled case. It would seem that the small perturbations in figure 19(a) grow to disrupt the relatively coherent interaction in figure 19(c), making it appear more like the other presumably less acoustically efficient structures. For the uncontrolled flow, the structure was reminiscent of the early stage of a vortex-tripling process suppressed by a similar control in a two-dimensional shear layer (Cavalieri *et al.* 2010). Further describing the evolution of the structure was, however, difficult due to rapid turbulent mixing and increasingly complex small-scale motions shown, for example, in figure 19(d).

At other azimuthal angles where the control is strong in figure 14(b), the control similarly adds perturbations to braid regions between two nearby vortices, as illustrated in figure 20(a,b).

These changes, which retarded-time estimates suggest would be loud events, did not only appear at θ matching the apparent θ -peaks of $C_{1,2,3}$. For example, at $\theta/\pi = 1/2$, the control shows no particularly strong peaks in figure 14(b). However, figure 21(b) shows a similar change to that observed in figure 19(a). The weak control seen in figure 14(b) near $\theta/\pi \approx -3/4$ prompted us to look first at this angle downstream; however even on the opposite side of the jet, a similar disruption was observed, as in figure 21(b), even though the control at $\theta/\pi = 1/2$ is much less pronounced (see figure 14a).

These observations suggest that the direct control effect on the jet near field targets the axisymmetric structure of the jet. This motivates figure 22(a,b), which shows the downstream evolution of the axisymmetric component of u'_x at the lipline $r/D = 0.5$. At $t \approx 10$ for both cases, a strong, axisymmetrically coherent structure becomes prominent at $x/D = 8$. Interestingly, based upon the estimated convection velocity $U_c/U_j = 0.66$, represented by the line to the C_1 control event, its onset would also be aligned with C_1 . Downstream, this axisymmetric disturbance becomes increasingly prominent. For $x/D \gtrsim 12$, it appears to significantly slow its streamwise advection,

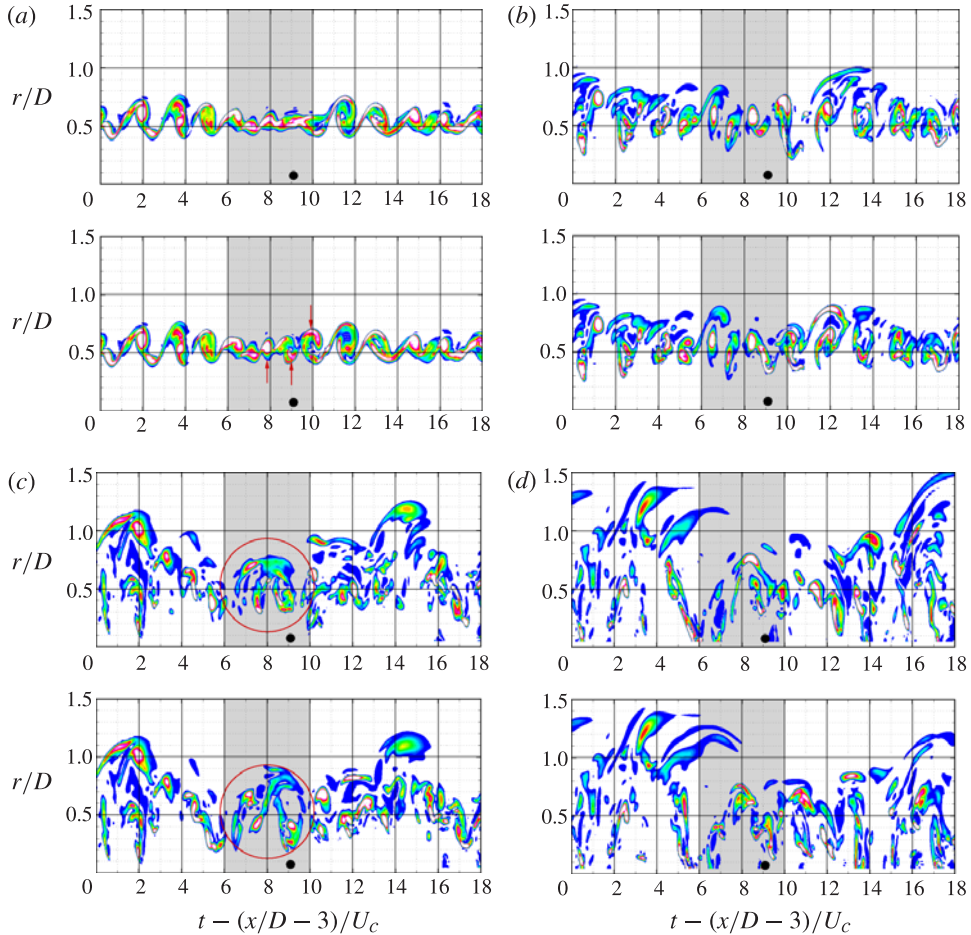


FIGURE 19. (Colour online) Instantaneous ω_θ contours at several streamwise locations: (a) $x/D=3$, (b) $x/D=4$, (c) $x/D=5$, (d) $x/D=6$; upper, uncontrolled; lower, controlled. The azimuthal angle at which ω_θ was measured corresponded to that of the control event C_3 . The black dot corresponds to the estimated time at which the large-amplitude peak of the control at $x/D=1.5$ arrives at $x/D=3$ (baseline). The shaded zone is used to highlight the time period when the control impact appears to be significant.

which might be important since a rapid change in the downstream advection of turbulence can constitute an efficient noise source. For the controlled jet, this structure is significantly less prominent, especially further downstream, presumably because of the $C_{1,2,3}$ control events which correspond to its apparent inception.

In considering these axisymmetric structures, it is noteworthy that the most significant sound suppression was also for $n=0$, as discussed in §5.2. The evidence from §5.3 suggested that the effect of the $C_{1,2,3}$ events persisted unexpectedly long in time. The slowed advection, estimated based upon this plot to be about $U_c/U_j = 0.33$, is a candidate mechanism for this, though it would be challenging to confirm definitively.

Instantaneous pressure iso-surfaces of $p/p_\infty = 0.98$ are shown in figure 23 before and after the control was applied. At $x/D \approx 13$, at $t=35$ (figure 23a) the uncontrolled jet exhibits a distinct vortex ring (see the arrow), which is removed for the controlled

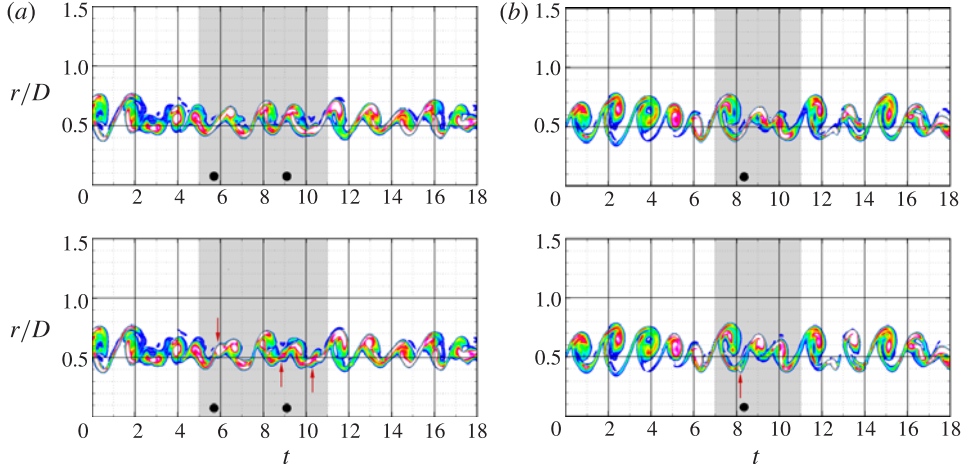


FIGURE 20. (Colour online) Instantaneous ω_θ contours at different azimuthal angles: (a) $\theta/\pi = -5/8$, (b) $\theta/\pi = 1$; upper, uncontrolled; lower, controlled. The arrows label the appearance of apparently new structures, caused by the control. The streamwise location is $x/D=3$. The black dots correspond to the estimated times at which the large-amplitude peaks of the control at $x/D=1.5$ arrive at $x/D=3$. The shaded zone is used to highlight the time period when the control impact appears to be significant.

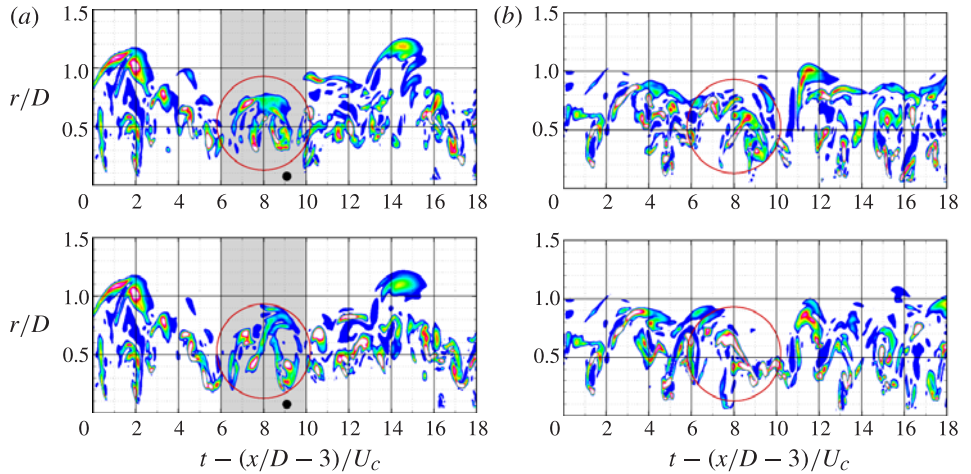


FIGURE 21. (Colour online) Instantaneous ω_θ contours at different azimuthal angles: (a) $\theta/\pi = -3/4$, (b) $\theta/\pi = 1/2$; upper, uncontrolled; lower, controlled. The streamwise location is $x/D=5$. The black dot corresponds to the estimated time at which the large-amplitude peak of the control at $x/D=1.5$ arrives at $x/D=3$. The shaded zone in (a) is used to highlight the time period when the control impact appears to be significant.

jet in the figure below. In figure 23(b), a similar observation is made at $t = 42$. The instantaneous pressure also supports the scenario that strong axisymmetric vortical structures were suppressed by the noise-reducing control. Visualizations of the corresponding sound waves (not shown here) demonstrate that they are indeed less intense (Kim 2012), but did not further illuminate any underlying mechanisms.

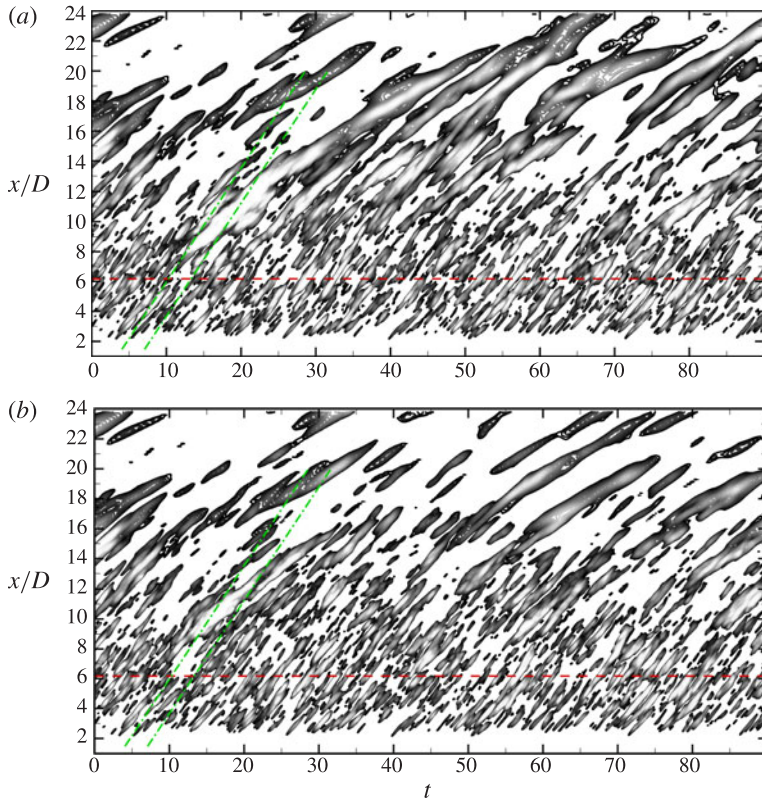


FIGURE 22. (Colour online) Space–time contours of the axisymmetric components of streamwise velocity fluctuations at the nozzle lip line: (a) uncontrolled; (b) controlled. The horizontal dashed line represents the average location where the potential core collapses. Two dashed-dot lines indicate the convection of the effects of the major control events C_1 and C_3 at the local convection velocity $U_c/U_j = 0.66$; the line corresponding to C_2 lies between these two lines.

5.5. Turbulence statistics

We see in figure 24(a) that the control causes the jet to spread more uniformly with downstream distance. For the time period simulated, the uncontrolled jet has approximately constant thickness for $10 \lesssim x/D \lesssim 13$, after which it continues to grow, initially somewhat faster. Figure 24(b) plots the same momentum thickness, but for every line search. Compared to the previous line searches, the streamwise growth of the controlled jet tends to become more and more linear. Harmonically excited shear layers are well known to show pauses in their streamwise growth when their structures merge (Ho & Huang 1982). The suppression of strong shear-layer vortex merging observed in §5.4 is consistent with such behaviour. Note that this particular pause is an artifact of the finite time of the control horizon we consider, reflecting the particular dynamics during the relatively short period. Averaging over the entire time series, before and after this control period, shows the distinctly linear profile expected for a high-speed turbulent jet.

The suppression of the axisymmetric structure is confirmed quantitatively in figure 25(a,b), which shows radially integrated azimuthal Fourier amplitudes of streamwise velocity fluctuations. For reference, we also show the integrated amplitude

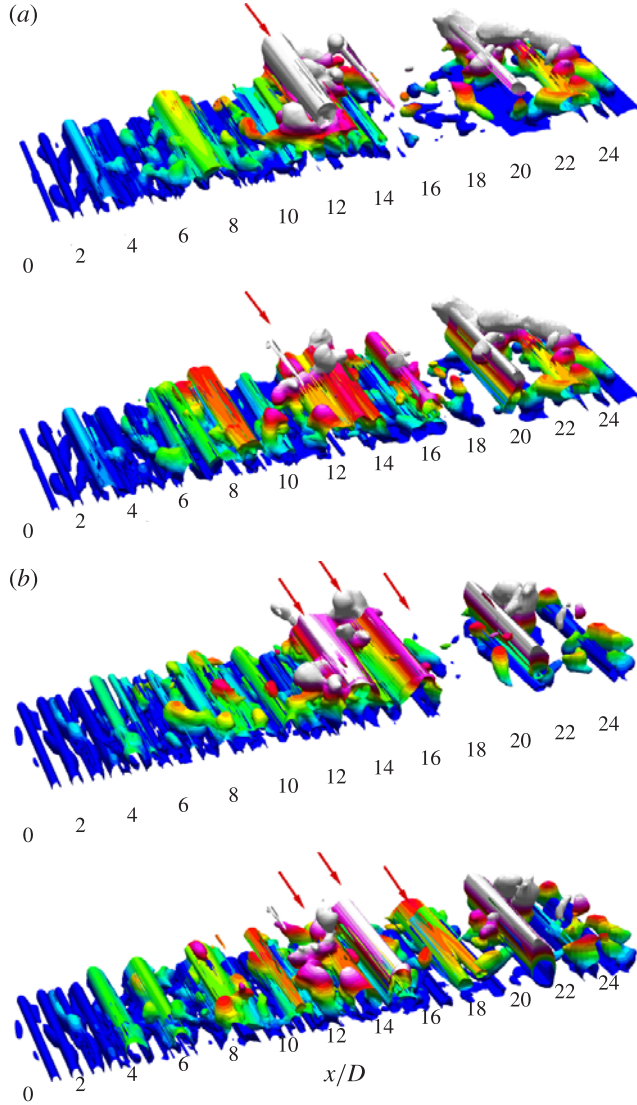


FIGURE 23. (Colour online) Instantaneous pressure iso-surfaces of $p=0.7$ for $r/D > 0.5$, rolled out in θ for before (a) and after (b) the control was applied at (a) $t=35$ and (b) $t=42$. The colours indicate the radial distance from the jet centreline.

of the uncontrolled jet calculated for the entire time period simulated in figure 26. The current jet demonstrates the expected character of a high-speed, high-Reynolds-number jet in that energy is distributed relatively uniformly to all the low-order Fourier components. For comparison, for example, see figure 14 of Kim & Choi (2009). All the low-order modes also exhibit a monotonic increase in amplitude (figure 26).

In figure 25(a), we see that the control particularly suppresses the $n=0$ mode, reducing it to the amplitude of the uncontrolled jet for the entire time period simulated, which also includes periods of relative quiet. Despite the θ locality of the control seen in figure 14(b), none of the $n > 1$ modes are significantly changed.

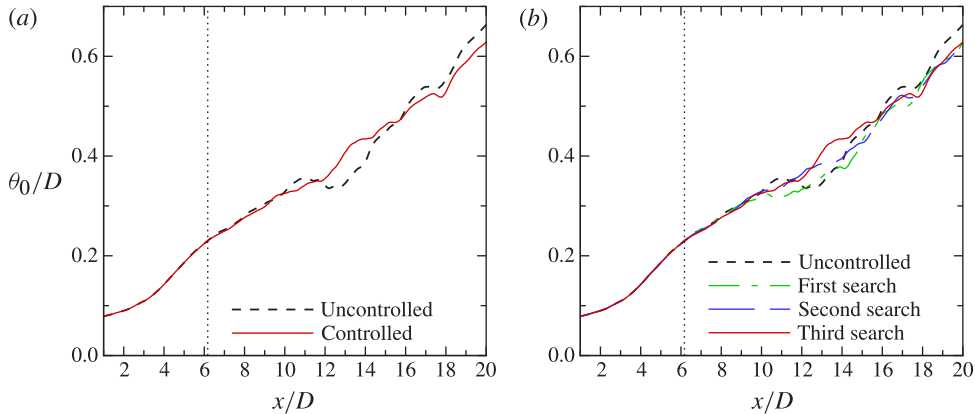


FIGURE 24. (Colour online) Streamwise growth of momentum thickness θ_0 for (a) the third line search and (b) every line search. Vertical dotted line denotes the average location at which the potential core closes.

The suppression of the $n = 0$ mode can also be seen in a proper orthogonal decomposition (POD) of the near-field pressure computed using standard methods discussed elsewhere (Freund & Colonius 2009; Kim 2012). The change in the modal energy with the control is compared in figure 27 for $n = 0$ and 1. Almost all changes occurred for $n = 0$, with the first two POD modes showing 36% and 33% reductions, respectively. The amplitude of the $n = 1$ mode shows only minor perturbations. The higher azimuthal modes show even smaller changes than $n = 1$ (Kim 2012).

In considering the implications of this, it should be emphasized that the $n = 0$ mode was not directly excited at the inflow (see §3.4), which indicates that the axisymmetric structures discussed in the previous section arise from nonlinear interactions in the jet shear layer. The control events appear to suppress this nonlinear interaction or disrupt these modes as they arise.

6. Concluding remarks

We have used adjoint-based optimization to identify a control that suppresses an acoustically efficient jet-noise source amongst the chaotic interactions in a turbulent jet. This is particularly noteworthy since the baseline jet, before application of control, matched experimental measurements. This approach is perhaps unique in that it provides specific guidance regarding adjustment toward noise suppression; it does not rely on any empirical trial-and-error iterations to suppress the sound. Tests confirmed that the efficacy of the optimized control is tied to its interactions with the instantaneous structures in the jet. When the optimization was applied to a time period of relatively little sound, the control did not achieve so significant a noise reduction (Kim 2012), with the interesting implication that the particularly loud events might be more controllable. Though control events were relatively local in the azimuthal coordinate around the nozzle lip, visualizations and turbulence statistics suggest that the control works primarily by disrupting acoustically efficient azimuthally correlated turbulence structures toward the end of the potential core. Standard Fourier spectral analysis and decomposition into POD modes showed that the axisymmetric $n = 0$ mode was suppressed with a corresponding modest increase in $n > 0$ mode energy, but this analysis did not point to any clear mechanism. Nothing so simple as the

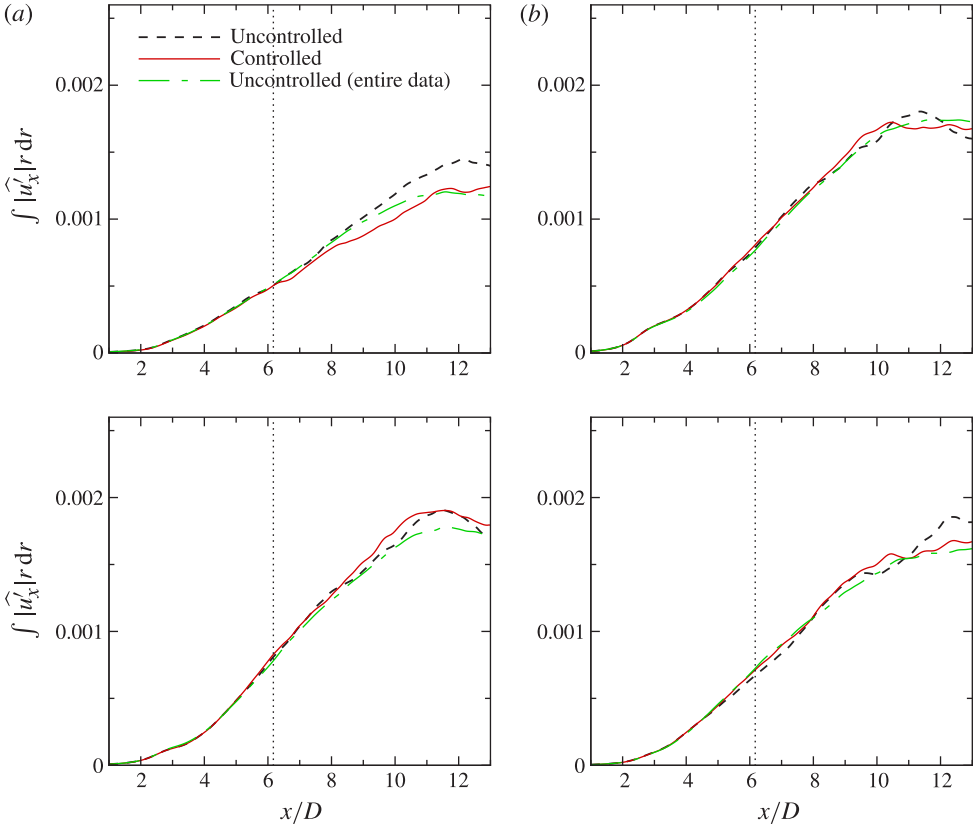


FIGURE 25. (Colour online) The streamwise growth of integrated azimuthal Fourier amplitudes: (a) $n = 0$; (b) $n = 1$; (c) $n = 2$; (d) $n = 3$. The vertical dotted line denotes the average location at which the potential core closes.

phasing and advection velocity perspective (Wei & Freund 2006) or the vortex tripling perspective (Cavalieri *et al.* 2010) from two dimensions was found (Kim 2012). While this perspective shows some of the mechanisms that might be responsible for noise and its reduction, clearly it has not yet provided that long-elusive phenomenological model discussed in the introduction capable of providing direct guidance for designing quieter jets. More work is needed on that long-standing problem.

The overall noise reduction was modest (~ 3.5 dB in a loudest direction), but particularly notable because it was identified by an automated procedure. It is unclear why the more significant noise reduction seen in the previous two-dimensional shear flow (Wei & Freund 2006) could not be reproduced, but we can speculate that the chaotic character of true turbulence presents a greater challenge for the control and the optimization process. It is well understood that correlation distances, for example, in turbulence are significantly shorter than in two-dimensional flows. This is expected to decrease the controllability of the downstream turbulence by actuation at the nozzle.

There are also potentially other factors that contribute to this challenge. While there is no means of making a direct comparison, coherence and intensity of two-dimensional flow structures are expected to enable them to be more acoustically

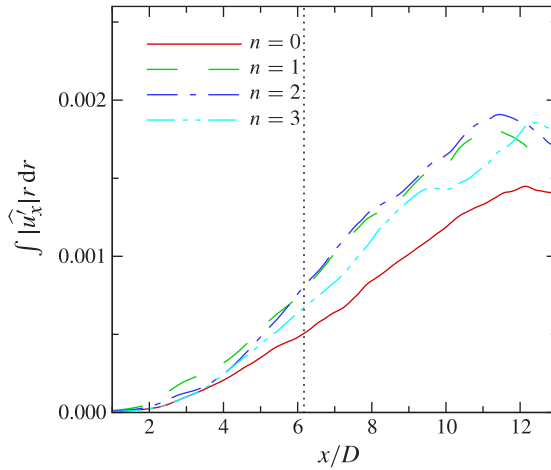


FIGURE 26. (Colour online) The streamwise growth of integrated Fourier amplitudes for the uncontrolled jet. Vertical dotted line denotes the average location at which the potential core closes.

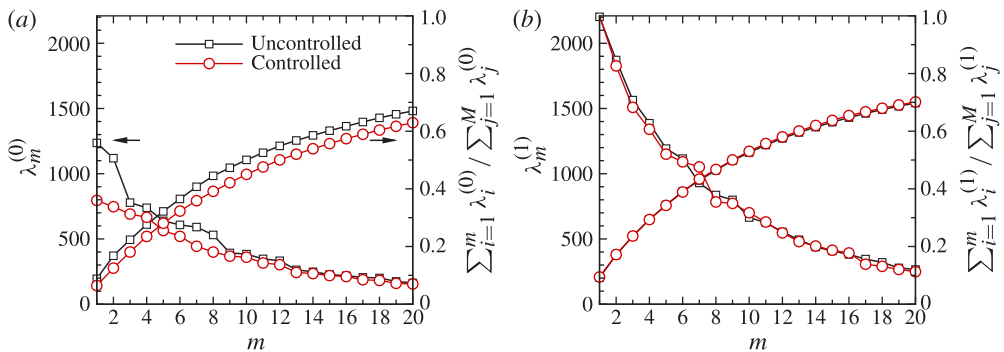


FIGURE 27. (Colour online) POD energetics before and after the control is applied: (a) $n=0$; (b) $n=1$.

efficient, and thereby perhaps more amenable to suppression as their downstream advection is regularized by control (Wei & Freund 2006).

Another potential challenge is the greater resolution needs of the present simulations. Large-eddy simulation by its nature typically challenges the limits of discrete resolution and also introduces additional modelling requirements. We confirmed mesh independence for all the reported statistical results, but errors introduced into the adjoint, either due to resolution or due to subgrid-scale models, could potentially limit its ability to suppress noise. It is noteworthy that large-scale interactions were altered by the small-scale, localized control events to suppress sound. However, we note that the noise suppression was comparable to that observed in a significantly more resolved direct numerical simulation of a turbulent plane mixing layer (Kleinman & Freund 2006). However, to properly assess this a DNS of a high enough Reynolds number would be required to provide both a realistic high-Reynolds-number jet and

one for which the subgrid-scale models would properly tested. This would be a substantial undertaking, and is beyond the scope of the current objectives.

It is possible that ~ 3.5 dB is near the limit of what can be achieved with modest-strength nozzle-located controls at fixed flow conditions, at least with a perturbation based upon the infinitesimal sensitivity of the basic flow as determined by the adjoint. It is possible that more iterations can reduce noise further, though the necessity of this would be an additional indication of the complexity of the problem, one that is unlikely to be described by a highly simplified model. Indeed, this level matches what has been achieved in empirical investigations with various noise-suppression technologies. In this study, we did not complete an optimization and find a minimum \mathcal{J} since, as discussed, that of itself was not a goal of the study and would require a much more significant amount of computation. The convergence rate suggests that additional reductions are possible, but that the route to any significantly quieter jet state is indirect. In contrast, the two-dimensional flow converged very quickly (Wei & Freund 2006), presumably due to the simplicity of the wave-packet-like structures in that low-dimensional study.

We close by emphasizing that the current control study was designed to understand the potential of such an approach and study jet-noise mechanics, rather than to optimize any particular actuator technology. Determining whether even adjoint-based optimization, such as we report, can identify practical noise suppression for jets at these speeds, will require additional investigation. However, since this procedure is relatively insensitive to the number of control parameters, we can anticipate that more complex flows might actually present greater opportunities for control. For example, it is well known that the noise from under-expanded jets can be sensitive to relatively small changes in nozzle configuration. Adjoint-based optimization should be well suited to such cases, so long as a predictive capability is available. Large-eddy simulation, such as used in the present study, would seem to hold the greatest promise for providing this since it provides an explicit representation of the flow unsteadiness at a range of scales that generates the most important noise.

Acknowledgements

We thank Professor M. Samimy at The Ohio State University for sharing the experimental data for validation. The first author appreciates Professor M. Wei for a useful discussion. We also gratefully acknowledge funding from NASA and the Office of Naval Research.

REFERENCES

- BERLAND, J., BOGEY, C., MARSDEN, O. & BAILLY, C. 2007 High-order, low dispersive and low dissipative explicit schemes for multiple-scale and boundary problems. *J. Comput. Phys.* **224** (2), 637–662.
- BEWLEY, T. R., MOIN, P. & TEMAM, R. 2001 DNS-based predictive control of turbulence: an optimal benchmark for feedback algorithms. *J. Fluid Mech.* **447**, 179–225.
- BODONY, D. J. 2006 Analysis of sponge zones for computational fluid mechanics. *J. Comput. Phys.* **212** (2), 681–702.
- BODONY, D. J. & LELE, S. K. 2005 On using large-eddy simulation for the prediction of noise from cold and heated turbulent jets. *Phys. Fluids* **17** (8), 085103.
- BODONY, D. J. & LELE, S. K. 2008 Low-frequency sound sources in high-speed turbulent jets. *J. Fluid Mech.* **617**, 231–253.
- BOGEY, C. & BAILLY, C. 2004 A family of low dispersive and low dissipative explicit schemes for flow and noise computations. *J. Comput. Phys.* **194** (1), 194–214.

- BOGEY, C. & BAILLY, C. 2006 Large eddy simulations of round free jets using explicit filtering with/without dynamic Smagorinsky model. *Intl J. Heat Fluid Flow* **27**, 603–610.
- BOGEY, C., BAILLY, C. & JUVÉ, D. 2003 Noise investigation of a high subsonic, moderate Reynolds number jet using a compressible large eddy simulation. *Theor. Comput. Fluid Dyn.* **16** (4), 273–297.
- BOGEY, C., MARSDEN, O. & BAILLY, C. 2012 Influence of initial turbulence level on the flow and sound fields of a subsonic jet at a diameter-based Reynolds number of 10^5 . *J. Fluid Mech.* **701**, 352–385.
- BRIDGES, J. E. & BROWN, C. A. 2004 Parametric testing of chevrons on single flow hot jets. *AIAA Paper* 2004-2824.
- BRIDGES, J. E. & WERNET, M. P. 2008 Turbulence associated with broadband shock noise in hot jets. *AIAA Paper* 2008-2834.
- CASALINO, D. 2003 An advanced time approach for acoustic analogy predictions. *J. Sound Vib.* **261** (4), 583–612.
- CAVALIERI, A. V. G., DAVILLER, G., COMTE, P., JORDAN, P., TADMOR, G. & GERVAIS, Y. 2011a Using large eddy simulation to explore sound-source mechanisms in jets. *J. Sound Vib.* **330** (17), 4098–4113.
- CAVALIERI, A. V. G., JORDAN, P., AGARWAL, A. & GERVAIS, Y. 2011b Jittering wave-packet models for subsonic jet noise. *J. Sound Vib.* **330** (18), 4474–4492.
- CAVALIERI, A. V. G., JORDAN, P., GERVAIS, Y., WEI, M. & FREUND, J. B. 2010 Intermittent sound generation and its control in a free-shear flow. *Phys. Fluids* **22**, 115113.
- CROW, S. C. & CHAMPAGNE, F. H. 1971 Orderly structure in jet turbulence. *J. Fluid Mech.* **48**, 547–591.
- ESCHRICHT, D., JORDAN, P., WEI, M., FREUND, J. & THIELE, F. 2007 Analysis of noise-controlled shear-layers. In *AIAA Paper* 2007-3660.
- FFOWCS WILLIAMS, J. E. 1963 The noise from turbulence convected at high speed. *Phil. Trans. R. Soc. Lond. A* **255** (1061), 469–503.
- FFOWCS WILLIAMS, J. E. & HAWKINGS, D. L. 1969 Sound generated by turbulence and surfaces in arbitrary motion. *Phil. Trans. R. Soc. Lond. A* **264** (1151), 321–342.
- FREUND, J. B. 1997 Proposed inflow/outflow boundary condition for direct computation of aerodynamic sound. *AIAA J.* **35** (4), 740–742.
- FREUND, J. B. 2001 Noise sources in a low-Reynolds-number turbulent jet at Mach 0.9. *J. Fluid Mech.* **438**, 277–305.
- FREUND, J. B. 2011 Adjoint-based optimization for understanding and suppressing jet noise. *J. Sound Vib.* **330** (17), 4114–4122.
- FREUND, J. B. & COLONIUS, T. 2009 Turbulence and sound-field POD analysis of a turbulent jet. *Intl J. Aeroacoust.* **8** (4), 337–354.
- FREUND, J. B., LELE, S. K. & MOIN, P. 2000 Numerical simulation of a Mach 1.92 turbulent jet and its sound field. *AIAA J.* **38** (11), 2023–2031.
- GAITONDE, D. V. & VISBAL, M. R. 1998 High-order schemes for Navier-Stokes equations: algorithm and implementation into FDL3DI. *AFRL-VA-WP-TR-1998-3060*. Air Force Research Laboratory, Wright-Patterson AFB.
- GOLDSTEIN, M. E. 2003 A generalized acoustic analogy. *J. Fluid Mech.* **488**, 315–333.
- GUDMUNDSSON, K. & COLONIUS, T. 2007 Spatial stability analysis of chevron jet profiles. *AIAA Paper* 2007-3599.
- HILEMAN, J. I. 2004 Large-scale structures and noise generation in high-speed jets. PhD thesis, Ohio State University, Columbus, Ohio.
- HILEMAN, J. & SAMIMY, M. 2001 Turbulence structures and the acoustic far field of a mach 1.3 jet. *AIAA J.* **39** (9), 1716–1727.
- HILEMAN, J. I., THUROW, B. S., CARABALLO, E. J. & SAMIMY, M. 2005 Large-scale structure evolution and sound emission in high-speed jets: real-time visualization with simultaneous acoustic measurements. *J. Fluid Mech.* **544**, 277–307.
- HO, C. M. & HUANG, L. S. 1982 Subharmonics and vortex merging in mixing layers. *J. Fluid Mech.* **119**, 443–473.

- JAMESON, A. 1988 Aerodynamic design via control theory. *J. Sci. Comput.* **3** (3), 233–260.
- JAMESON, A. 1995 Optimum aerodynamic design using CFD and control theory. *AIAA Paper* 1995-1729.
- JORDAN, P. & COLONIUS, T. 2013 Wave packets and turbulent jet noise. *Annu. Rev. Fluid Mech.* **45** (1), 173–195.
- JUVÉ, D., SUNYACH, M. & COMTE-BELLOT, G. 1980 Intermittency of the noise emission in subsonic cold jets. *J. Sound Vib.* **71** (3), 319–332.
- KARABASOV, S. A., AFSAR, M. Z., HYNES, T. P., DOWLING, A. P., MCMULLAN, W. A., POKORA, C. D., PAGE, G. J. & MCGUIRK, J. J. 2010 Jet noise: acoustic analogy informed by large eddy simulation. *AIAA J.* **48** (7), 1312–1325.
- KASTNER, J., SAMIMY, M., HILEMAN, J. & FREUND, J. B. 2006 Comparison of noise mechanisms in high and low Reynolds number high-speed jets. *AIAA J.* **44** (10), 2251–2258.
- KERHERVÉ, F., JORDAN, P., CAVALIERI, A. V. G., DELVILLE, J., BOGEY, C. & JUVÉ, D. 2012 Educing the source mechanism associated with downstream radiation in subsonic jets. *J. Fluid Mech.* **710**, 606–640.
- KIM, J. 2012 Adjoint-based control of turbulent jet noise. PhD thesis, University of Illinois at Urbana-Champaign.
- KIM, J. & CHOI, H. 2009 Large eddy simulation of a circular jet: effect of inflow conditions on the near field. *J. Fluid Mech.* **620**, 383–411.
- KIM, J. W. & LEE, D. J. 2000 Generalized characteristic boundary conditions for computational aeroacoustics. *AIAA J.* **38** (11), 2040–2049.
- KLEINMAN, R. R. & FREUND, J. B. 2006 Adjoint-based control of the noise from a turbulent mixing layer. *AIAA Paper* 2006-2501.
- KÆNIG, M., CAVALIERI, A. V. G., JORDAN, P., DELVILLE, J., GERVAIS, Y. & PAPAMOSCHOU, D. 2013a Farfield filtering and source imaging of subsonic jet noise. *J. Sound Vib.* **332** (18), 4067–4088.
- KÆNIG, M., CAVALIERI, A. V. G., JORDAN, P. & GERVAIS, Y. 2013b Jet noise control by fluidic injection from a rotating plug: linear and nonlinear sound source mechanisms. In *19th AIAA/CEAS Aeroacoustics Conference, Berlin, Germany*.
- LELE, S. K. 1992 Compact finite difference schemes with spectral-like resolution. *J. Comput. Phys.* **103** (1), 16–42.
- LIGHTHILL, M. J. 1952 On sound generated aerodynamically. I. General theory. *Proc. R. Soc. Lond. A* **211** (1107), 564–587.
- LILLY, D. K. 1992 A proposed modification of the Germano subgrid-scale closure method. *Phys. Fluids A* **4** (3), 633–635.
- LO, S. C., AIKENS, K. M., BLAISDELL, G. A. & LYRINTZIS, A. S. 2012 Numerical investigation of 3-d supersonic jet flows using large-eddy simulation. *Intl J. Aeroacoust.* **11** (7), 783–812.
- LUI, C. C. M. 2003 A numerical investigation of shock-associated noise. PhD thesis, Stanford University, Stanford, California.
- MAURY, R., KÆNIG, M., CATTAFESTA, L., JORDAN, P. & DELVILLE, J. 2012 Extremum-seeking control of jet noise. *Intl J. Aeroacoust.* **11** (3), 459–474.
- MENDEZ, S., SHOEBY, M., SHARMA, A., HAM, F. E., LELE, S. K. & MOIN, P. 2010 Large-eddy simulations of perfectly-expanded supersonic jets: quality assessment and validation. *AIAA Paper* 2010-271.
- MOIN, P., SQUIRES, K., CABOT, W. & LEE, S. 1991 A dynamic subgrid-scale model for compressible turbulence and scalar transport. *Phys. Fluids A* **3** (11), 2746–2757.
- POINSOT, T. J. & LELE, S. K. 1992 Boundary conditions for direct simulations of compressible viscous flows. *J. Comput. Phys.* **101**, 104–129.
- PRESS, W. H., FLANNERY, B. P., TEUKOLSKY, S. A. & VETTERLING, W. T. 1986 *Numerical Recipes*. Cambridge University Press.
- RIZZETTA, D. P., VISBAL, M. R. & BLAISDELL, G. A. 2003 A time-implicit high-order compact differencing and filtering scheme for large-eddy simulation. *Intl J. Numer. Meth. Fluids* **42**, 665–693.

- SAMIMY, M., KIM, J. H., KASTNER, J., ADAMOVICH, I. V. & UTKIN, Y. G. 2007 Active control of high-speed and high-Reynolds-number jets using plasma actuators. *J. Fluid Mech.* **578**, 305–330.
- SAMIMY, M., KIM, J. H., KEARNEY-FISCHER, M. & SINHA, A. 2010 Acoustic and flow fields of an excited high Reynolds number axisymmetric supersonic jet. *J. Fluid Mech.* **656**, 507–529.
- SHERER, S. E., VISBAL, M. R. & GALBRAITH, M. C. 2006 Automated preprocessing tools for use with a high-order overset-grid algorithm. *AIAA Paper* 2006-1147.
- SUHS, N. E., ROGERS, S. E. & DIETZ, W. E. 2002 Pegasus 5: An automated pre-processor for overset-grid CFD. *AIAA Paper* 2002-3186.
- TANNA, H. K. 1977 An experimental study of jet noise part I: Turbulent mixing noise. *J. Sound Vib.* **50** (3), 405–428.
- THOMAS, P. D. & LOMBARD, C. K. 1979 Geometric conservation law and its application to flow computations on moving grids. *AIAA J.* **17** (10), 1030–1037.
- THOMPSON, P. A. 1991 *Compressible-Fluid Dynamics*. McGraw-Hill.
- UZUN, A. & HUSSAINI, M. Y. 2009 Simulation of noise generation in the near-nozzle region of a chevron nozzle jet. *AIAA J.* **47** (8), 1793–1810.
- UZUN, A., LYRINTZIS, A. S. & BLAISDELL, G. A. 2004 Coupling of integral acoustics methods with LES for jet noise prediction. *Intl J. Aeroacoust.* **3** (4), 297–346.
- VINOKUR, M. 1974 Conservation equations of gasdynamics in curvilinear coordinate systems. *J. Comput. Phys.* **14** (2), 105–125.
- WEI, M. 2004 Jet noise control by adjoint-based optimization. PhD thesis, University of Illinois at Urbana-Champaign.
- WEI, M. & FREUND, J. B. 2006 A noise-controlled free shear flow. *J. Fluid Mech.* **546**, 123–152.
- ZAMAN, K. B., BRIDGES, J. E. & HUFF, D. L. 2011 Evolution from tabs to chevron technology—a review. *Intl J. Aeroacoust.* **10** (5), 685–710.